Supplementary Information
for

Electron spin resonance of single iron–phthalocyanine molecules and role of their non-localized spins in magnetic interaction

Xue Zhang[1,2], Christoph Wolf[1,2], Yu Wang[1,2], Hervé Aubin[3], Tobias Bilgeri[4], Philip Willke[1,2,5], Andreas J. Heinrich[1,6]* and Taeyoung Choi[1,6]*

1 Center for Quantum Nanoscience, Institute for Basic Science (IBS), Seoul 03760, Republic of Korea

2 Ewha Womans University, Seoul 03760, Republic of Korea

3 Universités Paris-Saclay, CNRS, Centre de Nanosciences et de Nanotechnologies, 91120, Palaiseau, France

4 Institute of Physics, École Polytechnique Fédérale de Lausanne, Station 3, CH-1015 Lausanne, Switzerland

5 Karlsruhe Institute of Technology, Karlsruhe 76131, Germany

6 Department of Physics, Ewha Womans University, Seoul 03760, Republic of Korea

Table of contents

1. Kondo splitting in varied external magnetic fields

Individual $[FePc]^{1-}$ molecule shows zero-bias peak in dI/dV spectrum measured by a non-magnetic tip at zero field, which is the signature of Kondo resonance (Supplementary Fig. 1(a)-(b)). By applying a magnetic field, the zero-bias peak splits into two excitation steps, corresponding to an inelastic excitation between the spin states with quantum number $m_s = +1/2$ and $m_s = -1/2$. The splitting indicates the Zeeman energy of the $[FePc]^{1-}$ spin, $E_{\mathrm{Zeeman}} = g\mu_{\mathrm{B}}B_{\mathrm{ex}}$ (μ_{B} is the Bohr magneton, B_{ex} is the magnetic field). The zero-bias peak splits in a similar way when the external field is along in-plane (B_{x}) and out-of-plane (B_{z}) direction. By fitting our dI/dV spectra with the scattering model proposed by Markus Ternes[46,47], we obtained the g-factors of 2.42±0.23 and 2.35±0.26 (error bars denoting the 95% confidence intervals) in B_{x} and B_{z}, respectively. Notably, the Kondo resonance can only be detected at molecule central area while the lobes are spectroscopically featureless.

Theoretically, the g-value extracted from a fit of the Kondo splitting, which is induced by Zeeman energy, should match the value obtained from ESR measurements. In the early theoretical work[31,32], the effective g-factor of the spin center under the presence of Kondo interaction can be described by: $g = g_0 - J_{sd}\rho(\varepsilon_F)$ in the "s-d" exchange model, where g_0 is g-factor of a free electron, J_{sd} represents the exchange coupling between the spin center and the conduction electrons, and $\rho(\varepsilon_F)$ is the density of states at the Fermi level. This implies that the effective g-factor can deviate from the value of a free electron due to an antiferromagnetic ($J_{sd} > 0$) or ferromagnetic ($J_{sd} < 0$) Kondo screening. Under a weak Kondo regime (J_{sd} is very small), which we anticipated for our system since the MgO insulating layers suppress the Kondo screening, the Kondo corrections to the g-factor should be very small. However, our extracted g-factor from Kondo splitting exhibits a much higher value than the free electron g-factor while the extracted g-factor from ESR shows very similar value with the free electron g-factor, which qualitatively match with the previous theoretical studies in the weak Kondo regime. On the other hand, the energy resolution (ΔE) of a STM dI/dV measurement is subject to broadening caused by system temperature and externally applied modulation voltage, where ΔE becomes $\sqrt{(3k_BT)^2 + (2.5eV_{mod})^2}$. In our experimental conditions, ΔE is approximately 0.5 meV at a temperature of ~2 K and V_{mod} of ~0.1 mV. This value from experimental broadening is, however, comparable with the one of the Kondo splitting. In contrast, we can readily obtain an energy resolution of 0.2 μeV using ESR detection, allowing much precise measurement of the g-factor although our system temperature is ~2 K.

The magnetic properties of $[FePc]^{1-}$ anions have been thoroughly studied in bulk systems [Ref. 30]. However, the previous work was performed in a crystal form, containing Na^+, C_{70}^-, and solvent molecules, which is a very complicated chemical environment compared to our studies on well-isolated individual $[FePc]^-$ molecule adsorbed on insulating layers. Also, the previous bulk $[FePc]^{1-}$ system doesn't have any Kondo screening and/or Kondo effect. In addition, the fitted g-factors from the dI/dV spectra have relatively large error bars. Therefore, it is not trivial to directly compare the g-factor values of the previous one with our measurement. The high magnetic field required by dI/dV measurement may also bring unexpected polarization of the central Fe atom, causing inaccuracy when evaluating the g-factor. However, we have not found clear evidence on this in both experiment and DFT calculation.

In summary, the theoretically predicted deviation of g-factor under a Kondo screening, difference of experimental environments, and significant error bars in the evaluation of Kondo

splitting indicate that the g-factor extracted from ESR measurement compared to dI/dV is more precise and reliable in our experimental conditions.

Supplementary Fig. 1(c) displays the dI/dV measured on an individual $[FePc]^{1-}$ with a spin-polarized tip, showing the asymmetry around zero bias. The asymmetric feature in dI/dV results from the selection rule that the total spin angular momentum is conserved for the spin excitation during a tunneling process[48,49]. Thus, it requires different spin states of the tunneling electron either from the tip or the substrate to excite the spin under the tip at different bias polarities. Relying on the degree of the tip polarization, the relative amounts of the electrons from the states to surface spin are different. In consequence, an asymmetry appears in the dI/dV curve. The decline of the dI/dV spectra at large bias is caused by the spin-pumping effect that the higher tunneling current pumps the spin to be more in its excited state and results in a change in the conductance.

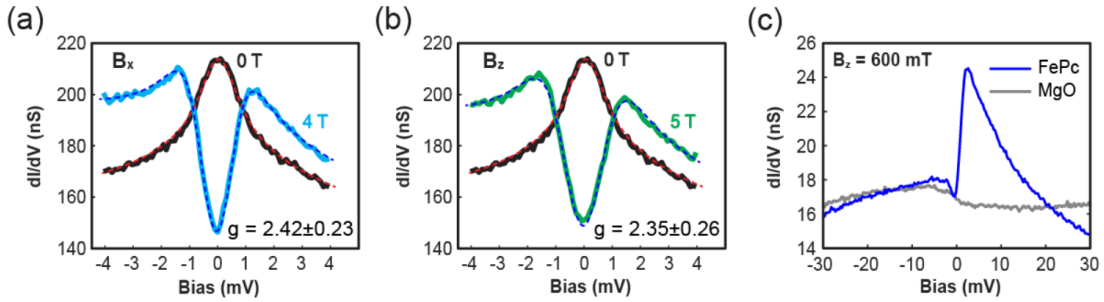

Supplementary Fig. 1 | (a)(b) dI/dV spectra showing Kondo resonance at zero field (black lines) and splitting in an (a) in-plane field, B_x (blue line) and (b) out-of-plane field, B_z (green line). The dashed lines are the fits based on the scattering model proposed by Markus Ternes. Tip was positioned at the center of $[FePc]^{1-}$. The errors (error bars) shown here and throughout the whole Supplementary Information denote the 95% confidence intervals obtained from the non-linear fits, unless stated specifically. (c) dI/dV spectra taken with a spin-polarized tip above the center of $[FePc]^{1-}$ and a bare MgO area at B_z = 600 mT. Spectroscopy conditions: (a)(b) Tip was set as V = 4 mV, I_{set} = 700 pA before disabling the feedback and a modulated voltage V_{mod} = 0.1 mV was applied; (c) V = -30 mV, I_{set} = 500 pA, V_{mod} = 1 mV. All dI/dV measurements were performed at the STM temperature of 1.7 K.

2. Extraction of μ_{FePc} by using different methods and in different magnetic fields

According to the equation (2) in the main text, the magnetic moment of $[FePc]^{1-}$ (μ_{FePc}) can be extracted by fitting either $f_0 \propto B_{tip}(I)$ or $f_0 \propto B_z$. We thus compared the μ_{FePc} deduced by these two methods. Supplementary Fig. 2(a) shows the ESR spectra measured with varied tunneling current (I_{set}) in a given out-of-pane (B_z) external field. The change of resonance frequency as a function of I_{set} is plotted in Fig. S2(b), yielding μ_{FePc} of 1.008±0.001 μ_B, in good agreement with the g-factors measured in Supplementary Section 1. Supplementary Fig. 2(c)-(d) are results of external field dependence ESR spectra taken at same I_{set}. The fitting gives μ_{FePc} of 0.959±0.010 μ_B. The magnetic moment obtained by varied-current and varied-external field ESR measurements show a deviation of less than 5%. This deviation is likely from the overestimated exchange coupling interaction between the tip and the underneath spin when the tip is infinitely far (i.e. when I_{set} = 0). In this extreme limit, the tip field may deviate from the linear relation with the tunneling current setpoint, leading to a

slight deviation in the μ_{FePc} extracted from the varied-current measurements compared to the varied-external field measurements. However, the coupling energy of $[\mathrm{FePc}]^{1-}$ dimers are not subject to the absolute value of the magnetic moments and within this deviation and we could still utilize the tip field as a control of the local magnetic field.

In addition, we found that the magnetic moment of individual $[\mathrm{FePc}]^{1-}$ molecules was nearly isotropic in different directions of the external magnetic field. Supplementary Figs. 2(e)-(h) show the ESR measurements performed in in-plane external magnetic field (B_{x}). We measured a μ_{FePc} of also approximately 1 μ_{B}, similar to the one obtained in B_{z} field. The less than 5% deviation between $\mu^{\mathrm{z}}_{\mathrm{FePc}}$ and $\mu^{\mathrm{x}}_{\mathrm{FePc}}$ may stem from the inhomogeneous spin occupied orbital configuration along different directions.

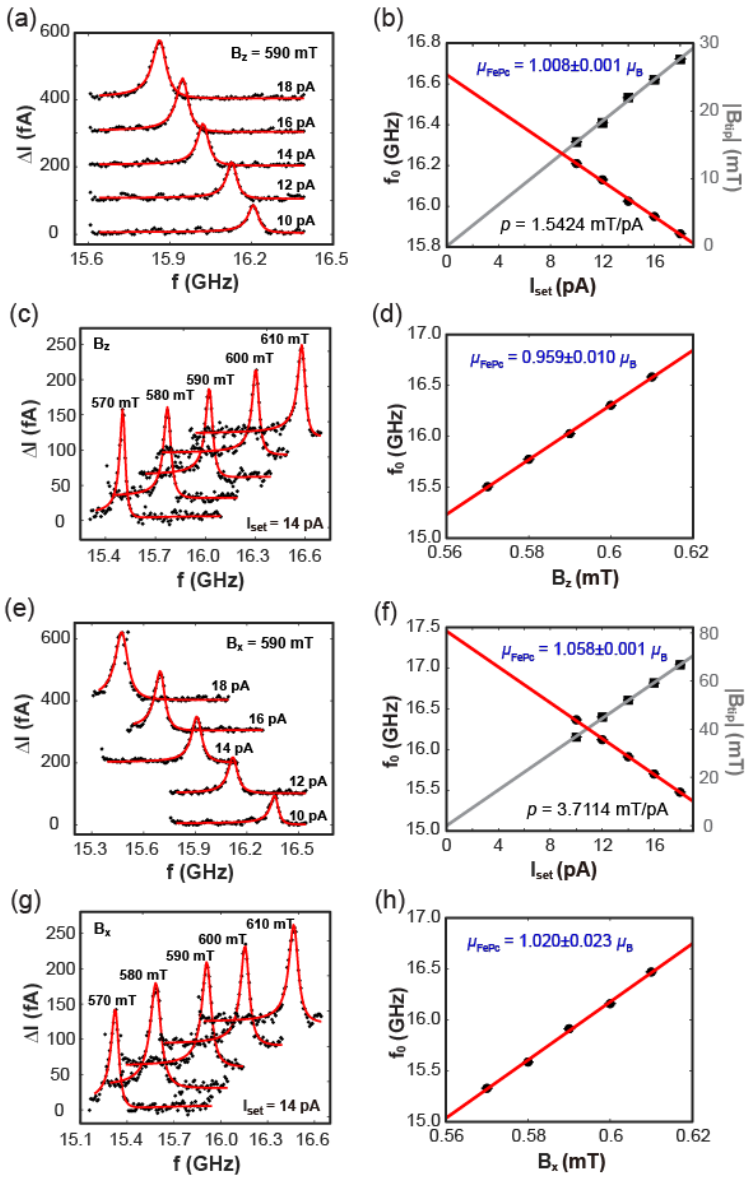

Supplementary Fig. 2 | (a)(b) Current-dependence ESR spectra measured in out-of-plane field B_{z} = 590 mT. The linear fit of resonance frequencies as a function of current yields the magnetic moment of $[\mathrm{FePc}]^{1-}$ which is 1.008±0.001 μ_{B}. In addition, the corresponding tip field at a given current can be described by a conversion coefficient which is p = 1.5424 mT/pA. (c)(d) External field dependence ESR

spectra measured in different out-of-plane fields with the same tunneling current setpoint, showing μ_{FePc} = 0.959±0.010 μ_{B}. (e)(f) Current-dependence ESR spectra measured in in-plane field B_{x} = 590 mT, giving the magnetic moment of $[\mathrm{FePc}]^{1-}$ of 1.058±0.001 μ_{B}. (g)(h) External field dependence ESR spectra measured in different B_{x} (in-plane field) with the same tunneling current setpoint, showing μ_{FePc} = 1.020±0.023 μ_{B}. All ESR measurements were performed with the same spin-polarized tip and on same $[\mathrm{FePc}]^{1-}$ molecule. ESR conditions: V = 100 mV, V_{rf} = 40 mV.

3. Statistics on magnetic moment of different individual $[\mathrm{FePc}]^{1-}$ molecules

Figure 1(d) in the main text demonstrates the magnetic moment extracted by tip field dependence ESR measurements in a given B_{z} field. We then measured ESR on the same $[\mathrm{FePc}]^{1-}$ molecule with the same tip in varied B_{z} fields at a given tip field (same tunneling current). As shown in Fig. S3(a), by fitting f_0 linearly to B_{z}, we obtained a μ_{FePc} of 0.950±0.048 μ_{B}, which is very close to the value measured by tip field dependence measurements.

Supplementary Fig. 3(b) plots the magnetic moments of different individual $[\mathrm{FePc}]^{1-}$ molecules extracted from varied tip field measurements in fixed external magnetic fields, giving an averaged magnetic moment of 1.028±0.023 μ_{B}.

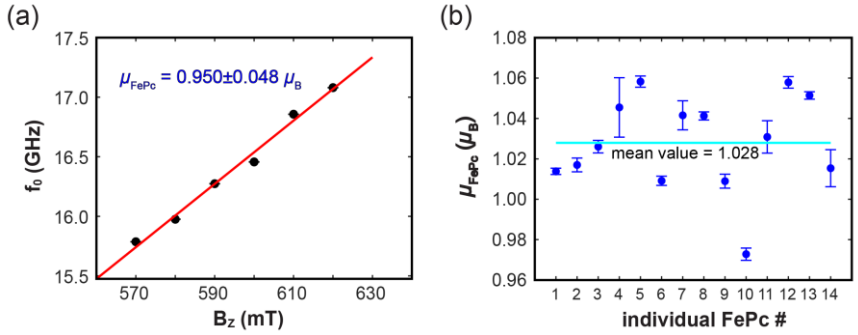

Supplementary Fig. 3 | (a) Resonance frequency shift as a function of external magnetic field at given tip field (I_{set} = 15 pA) with same tip and on same $[\mathrm{FePc}]^{1-}$ molecule as measured in Fig. 1(c). ESR conditions: V = 100 mV, V_{rf} = 10 mV. (b) Magnetic moments of 14 individual $[\mathrm{FePc}]^{1-}$ molecules obtained by tip field dependence ESR measurements in given external magnetic fields.

4. Current-dependence ESR spectra of different $[\mathrm{FePc}]^{1-}$-$[\mathrm{FePc}]^{1-}$ dimers and statistics on coupling energy

In our experiments, we found abundant naturally formed $[\mathrm{FePc}]^{1-}$ clusters. The majority was $[\mathrm{FePc}]^{1-}$-$[\mathrm{FePc}]^{1-}$ dimer and two favored adsorption configurations were found, namely (3, 4) and (0, 5) by counting the oxygen lattices passing between two Fe centers. The center-center distance for (3, 4) and (0, 5) dimers are exactly the same. Occasionally, we found (2, 5) dimers but much fewer in numbers. In these dimers, each ligand prefers to orient to (2, 1) direction, as illustrated by the black arrows in Supplementary Fig. 4(a), (d), and (g). Moreover, the two nearest aromatic rings belonging to two molecules are also arranged in (2, 1) configuration (*i.e.* the heads of the two black arrows are apart by 2×1 oxygen atoms). This is consistent with the optimized adsorption configuration of a $[\mathrm{FePc}]^{1-}$-$[\mathrm{FePc}]^{1-}$ dimer by DFT calculations. The relative possibility of finding these dimers is 38%, 53%, 9% for (3, 4), (0, 5), (2, 5), respectively

(Fig. S5). The coupling energy is similar when the tip is positioned on any molecule within the dimer. The comparison of current dependence ESR spectra and coupling energy measured on each molecule in the dimers are shown in Supplementary Fig. 4(b), (c), (e), (f), (h), and (i).

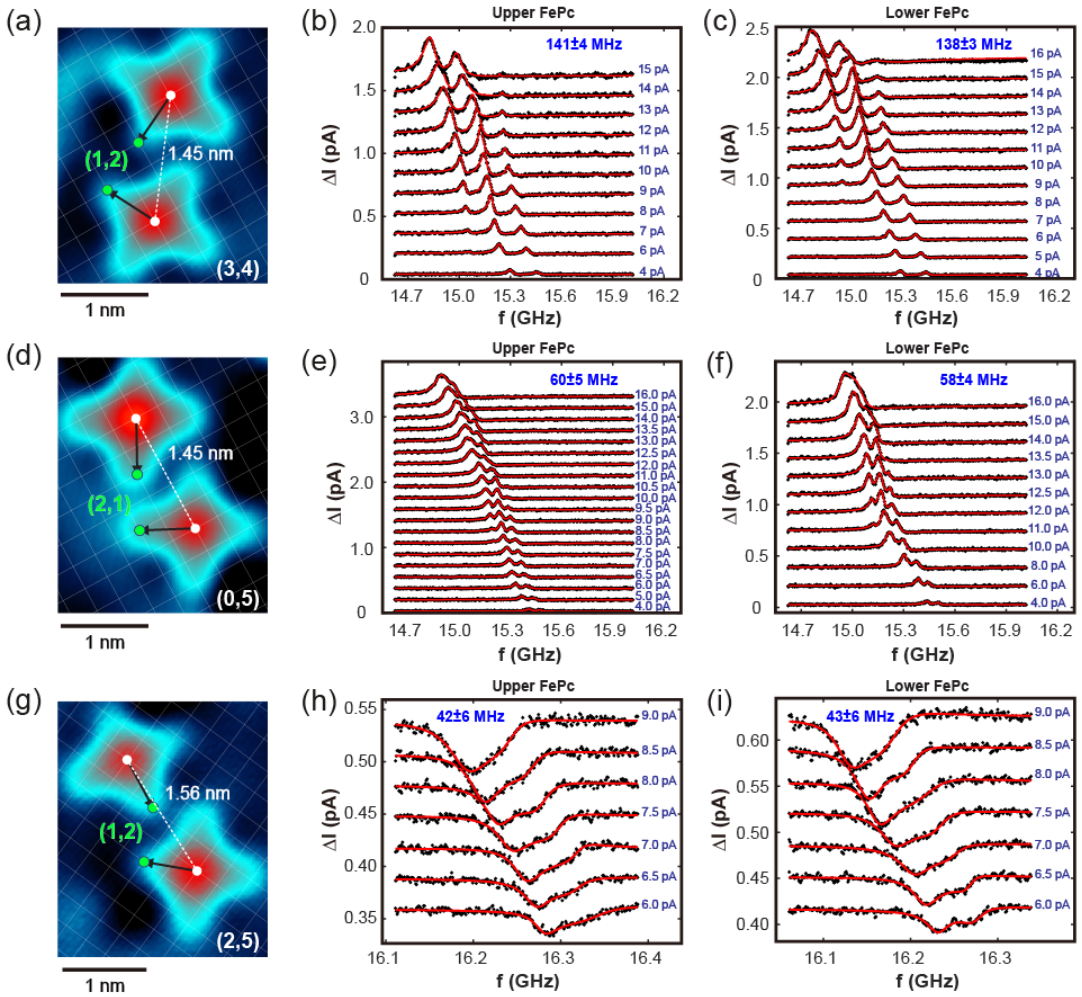

Supplementary Fig. 4 | (a)(d)(g) STM images of (3, 4), (0, 5), and (2, 5) dimer. Dashed white lines connect two Fe centers. Black arrows (start from the Fe center and end at the oxygen atom underneath the aromatic ring) indicate the relative alignment of molecular ligands. In these dimers, the two nearest aromatic rings belonging to two molecules are apart by 2×1 oxygen lattices, as highlighted by green coordinates. The middle and right columns exhibit current dependence ESR spectra measured on both molecules in a dimer. Coupling energy obtained by measuring ESR splitting is labelled on the top of each panel. Scanning conditions: (a)(d) V = 180 mV, I_{set} = 20 pA; (g) V = 150 mV, I_{set} = 8 pA. ESR conditions: V = 100 mV, (b)(c) V_{rf} = 50 mV, B_z = 550 mT; (e)(f) V_{rf} = 40 mV, B_z = 550 mT; (h)(i) V_{rf} = 25 mV, B_z = 570 mT. The ESR spectra have been vertically shifted one after another by (b) 150 fA; (c) 170 pA; (e)(f) 170 pA; (h)(i) 70 pA for clarity.

By measuring 31 molecules in a configuration of either (3, 4), (5, 0) or (2, 5), we obtained average coupling energy (J+D) for (3, 4), (0, 5) and (2, 5) dimer of 134±19 MHz, 64±7 MHz, and 42±6 MHz, respectively (Supplementary Fig. 5). The dipolar contribution D is estimated

by considering two point spins with 1 μ_B and has a value of 17 MHz for (3, 4) and (0, 5) dimers and 14 MHz for (2, 5) dimer. As demonstrated in Fig. 3, the change in coupling energy for different dimer configurations is a result of different ligand-ligand distance. In addition, the less occurrence of (3, 4) configuration than (0, 5) configuration may imply the subtle difference between these two configurations which are caused by different adsorption energy, although it is difficult to distinguish from the topography image.

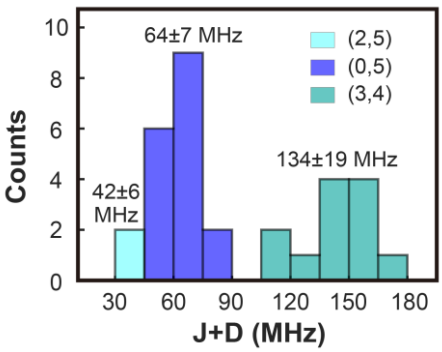

Supplementary Fig. 5 | Statistics of $[FePc]^{1-}$-$[FePc]^{1-}$ dimer configurations and corresponding ESR splitting. In all these measurements, only an out-of-plane field was applied. The errors shown on different color bricks are from the statistical standard deviations of the coupling energy measured on all dimers of the same configuration.

5. ESR transitions in Heisenberg two-spin system with the tip field detuning effect

In our experiment, the Zeeman energy (~16 GHz) set by external magnetic field is much stronger than the intermolecular coupling energy (~100 MHz). This implies that $[FePc]^{1-}$ spins are aligned to the direction of the external field. Thus, we can solve the Hamiltonian in equation (3) by using Zeeman basis $|00\rangle, |01\rangle, |10\rangle$, and $|11\rangle$. $|0\rangle$ and $|1\rangle$ are eigenvectors of spin operator $\boldsymbol{S}$ along the external field direction of first and second spin, respectively. Due to the existence of inter-spin coupling, two of the eigenstates, represented as $|-\rangle$ and $|+\rangle$, become a linear superposition of states $|01\rangle$ and $|10\rangle$, as shown below while $|00\rangle$ and $|11\rangle$ remain the other two eigenstates of Hamiltonian in equation (3):

$$|-\rangle = -\frac{\alpha}{\sqrt{\alpha^2+1}}|01\rangle + \frac{1}{\sqrt{\alpha^2+1}}|10\rangle,$$

$$|+\rangle = \frac{1}{\sqrt{\alpha^2+1}}|01\rangle + \frac{\alpha}{\sqrt{\alpha^2+1}}|10\rangle$$

where α indicates the relative weight of $|01\rangle$, $|10\rangle$ components in the $|-\rangle$ and $|+\rangle$ states, $\alpha = \frac{2(\mu_1-\mu_2)B_{ex}+2\mu_1 B_{tip}+\sqrt{\left[J-\frac{D}{2}(1-3\cos^2\theta)\right]^2+\left[2(\mu_1-\mu_2)B_{ex}+2\mu_1 B_{tip}\right]^2}}{J-\frac{D}{2}(1-3\cos^2\theta)}$.

The eigenenergies for $|00\rangle$, $|-\rangle$, $|+\rangle$ and $|11\rangle$ are:

$$E_{00} = \frac{1}{4}h[J + D(1-3\cos^2\theta)] - \left(\mu_1 B_{\mathrm{ex}} + \mu_1 B_{\mathrm{tip}} + \mu_2 B_{\mathrm{ex}}\right)$$

$$E_{-} = -\frac{1}{4}h[J + D(1-3\cos^2\theta)] - \frac{1}{2}\sqrt{h^2\left(J - \frac{1}{2}D(1-3\cos^2\theta)\right)^2 + 4\left(\mu_1 B_{\mathrm{ex}} + \mu_1 B_{\mathrm{tip}} - \mu_2 B_{\mathrm{ex}}\right)^2}$$

$$E_+ = -\frac{1}{4}h[J + D(1 - 3\cos^2\theta)] + \frac{1}{2}\sqrt{h^2\left(J - \frac{1}{2}D(1 - 3\cos^2\theta)\right)^2 + 4\left(\mu_1 B_{ex} + \mu_1 B_{tip} - \mu_2 B_{ex}\right)^2}$$

$$E_{11} = \frac{1}{4}h[J + D(1 - 3\cos^2\theta)] + \left(\mu_1 B_{\mathrm{ex}} + \mu_1 B_{\mathrm{tip}} + \mu_2 B_{\mathrm{ex}}\right)$$

Since we have assumed the first spin is the one under the tip, ESR transition is only allowed when the quantum number m_s of this spin is changed by $\Delta m_s = \pm 1$. Therefore, possible ESR transitions are $|00\rangle \rightarrow |-\rangle$, $|+\rangle \rightarrow |11\rangle$, $|00\rangle \rightarrow |+\rangle$ and $|-\rangle \rightarrow |11\rangle$. Corresponding frequencies of these transitions are given by:

$$f_1 = \frac{E_- - E_{00}}{h} = -\frac{1}{2}[J + D(1 - 3\cos^2\theta)] + \frac{1}{h}(\mu_1 B_{\mathrm{ex}} + \mu_1 B_{\mathrm{tip}} + \mu_2 B_{\mathrm{ex}}) - \frac{1}{2}\sqrt{\left(J - \frac{1}{2}D(1 - 3\cos^2\theta)\right)^2 + \frac{4}{h}\left(\mu_1 B_{\mathrm{ex}} + \mu_1 B_{\mathrm{tip}} - \mu_2 B_{\mathrm{ex}}\right)^2}$$

$$f_2 = \frac{E_{11} - E_+}{h} = \frac{1}{2}[J + D(1 - 3\cos^2\theta)] + \frac{1}{4\pi}(\mu_1 B_{\mathrm{ex}} + \mu_1 B_{\mathrm{tip}} + \mu_2 B_{\mathrm{ex}}) - \frac{1}{2}\sqrt{\left(J - \frac{1}{2}D(1 - 3\cos^2\theta)\right)^2 + \frac{4}{h}\left(\mu_1 B_{\mathrm{ex}} + \mu_1 B_{\mathrm{tip}} - \mu_2 B_{\mathrm{ex}}\right)^2}$$

$$f_3 = \frac{E_+ - E_{00}}{h} = -\frac{1}{2}[J + D(1 - 3\cos^2\theta)] + \frac{1}{h}\left(\mu_1 B_{\mathrm{ex}} + \mu_1 B_{\mathrm{tip}} + \mu_2 B_{\mathrm{ex}}\right) + \frac{1}{2}\sqrt{\left(J - \frac{1}{2}D(1 - 3\cos^2\theta)\right)^2 + \frac{4}{h}\left(\mu_1 B_{\mathrm{ex}} + \mu_1 B_{\mathrm{tip}} - \mu_2 B_{\mathrm{ex}}\right)^2}$$

$$f_4 = \frac{E_{11} - E_-}{h} = \frac{1}{2}[J + D(1 - 3\cos^2\theta)] + \frac{1}{h}\left(\mu_1 B_{\mathrm{ex}} + \mu_1 B_{\mathrm{tip}} + \mu_2 B_{\mathrm{ex}}\right) + \frac{1}{2}\sqrt{\left(J - \frac{1}{2}D(1 - 3\cos^2\theta)\right)^2 + \frac{4}{h}\left(\mu_1 B_{\mathrm{ex}} + \mu_1 B_{\mathrm{tip}} - \mu_2 B_{\mathrm{ex}}\right)^2}.$$

We note that α depends on δ, meaning the dominant ESR transitions vary at different tip fields. Since the tip field direction in our work is always opposite to the external field, B_{tip} naturally contains a negative sign with respect to B_{ex}. In the weak tip field regime, i.e. $B_{\mathrm{tip}} \approx 0$, yielding $\delta > 0$ and $\alpha > 1$. Hence, $|01\rangle$ and $|10\rangle$ are the dominant components of $|-\rangle$ and $|+\rangle$ states, respectively, leading to prevailed f_3 (from E_{00} to E_+) and f_4 (from E_- to E_{11}). In comparison, when the tip field is strong, i.e. $B_{\mathrm{tip}} \ll 0$, it yields $\delta < 0$ and $\alpha < 1$ which means $|-\rangle$ and $|+\rangle$ state have more weight on $|10\rangle$ and $|01\rangle$, respectively. As a result, f_1 (from E_{00} to E_-) and f_2 (from E_+ to E_{11}) are more prominent while the other two transitions are almost vanishing. When B_{tip} cancels the difference of Zeeman energy of two $[\mathrm{FePc}]^{1-}$ spins (meaning $\delta = 0$, $\alpha = 1$), $|10\rangle$ and $|01\rangle$ are equally weighted in $|-\rangle$ and $|+\rangle$, f_1 and f_4 have the same intensity and f_2, f_3 merge to one peak (when dipolar coupling contribution is much smaller than exchange coupling contribution), as indicated by the white arrows in Fig. 2(a,iii) and 2(b,iii).

In the strong tip field regime of both $[FePc]^{1-}$ dimers, we found that the ESR signal at f_1 driving the transition from $|00\rangle$ to $|10\rangle$ appears at lower frequency than the one at f_2 driving the transition from $|01\rangle$ to $|11\rangle$. This implies that the $|10\rangle$ state is energetically favorable compared to the $|11\rangle$ state. In addition, the fitted J value based on the model Hamiltonian gives a positive number. These results indicate that the exchange interaction of the two $[FePc]^{1-}$ molecules prefers to be antiferromagnetically (AFM) coupled for both (3, 4) and (0, 5) dimers.

For a given two-spin system where μ_1, μ_2, B_{ex}, J, D, and θ are known, the energy of each state can be plotted as a function of B_{tip}, as shown in Supplementary Fig. 6(a). Here, we used the approximate experimental values for each parameter: $\mu_1 = 1.02\ \mu_B$, $\mu_2 = 0.98\ \mu_B$, $B_{ex} =$ 550 mT, $J =$ 150 MHz, $D =$ 15 MHz, θ is 90° (meaning with an out-of-plane field only). As illustrated by Fig. 1, the tip field in our case had an opposite direction compared to external magnetic field, so B_{tip} was set to vary from -60 mT to 0. Supplementary Fig. 6(b) presents the four ESR transitions derivated from Supplementary Fig. 6(a). Taking the thermal population of each state into account (*i.e.* at a STM temperature of T = 1.7 K) and with a reasonable linewidth $\Gamma =$ 30 MHz, we were able to simulate the ESR signal in frequency sweep at different tip fields, as shown in Supplementary Fig. 6(c).

In the simulations, the amplitudes of the resonances are obtained from the usual quantum formula $p = |\langle F|S_{x1}|I\rangle|^2$ for the probability of the transition between the initial $|I\rangle$ and final state $|F\rangle$ induced by the spin operator S_{x1} acting only on spin 1. Only this operator S_{x1} is included in the formula as only the spin 1 located below the tip is driven by the microwave signal. The initial and final eigenstates $|I\rangle$, $|F\rangle$ correspond to one of the four eigenstates $|00\rangle$, $|-\rangle$, $|+\rangle$ and $|11\rangle$.

From this formula, one sees that the transition probability is non-zero only for transitions involving a change of $\Delta m_{z1} = \pm 1$ for spin 1.

As the four identified resonances, f_1 to f_4, involve the mixed states $|-\rangle$ and $|+\rangle$, the transitions amplitudes will depend on the coefficient α, which is the relative weight of the $|01\rangle$ and $|10\rangle$ components in the mixed states $|-\rangle$ and $|+\rangle$ where the value of α is controlled by the tip field (B_{tip}).

As an example, for the resonant transition f_1 between the ground state $|00\rangle$ and the singlet state $|-\rangle$, the transition amplitude is given by:

$$A = |\langle -|S_{x1}|00\rangle|^2.$$

And using the expression given in the manuscript for the singlet state $|-\rangle$, we can obtain:

$$A = \frac{\alpha^2}{\alpha^2+1}|\langle 01|S_{x1}|00\rangle|^2 + \frac{1}{\alpha^2+1}|\langle 10|S_{x1}|00\rangle|^2.$$

Furthermore, using $\langle 01|S_{x1}|00\rangle = 0$, $\langle 10|S_{x1}|00\rangle = \frac{1}{2}$ and $\alpha = \frac{\delta+\sqrt{\varepsilon^2+\delta^2}}{\varepsilon}$ the transition amplitude can be written as: $A = \frac{1}{8}\frac{1}{1+\frac{\delta}{\varepsilon}\sqrt{1+\left(\frac{\delta}{\varepsilon}\right)^2}+\left(\frac{\delta}{\varepsilon}\right)^2}$.

For $B_{tip} \ll 0$: $\delta \ll \varepsilon$, the mixed state $|-\rangle \approx |10\rangle$ and the amplitude $A \to 1/8$.

For $B_{tip} \gg 0$: $\delta \gg \varepsilon$, the mixed state $|-\rangle \approx |01\rangle$ and the amplitude $A \to 0$.

This shows that the transition amplitude is proportional to the relative weight of the $|10\rangle$ component in the mixed state.

Moreover, fitting the experimentally measured f_1, f_2, f_3 and f_4 (Fig. 2(a,iii) and (b,iii))

as a function of tip field based on above equations (the overlapped dashed curves in Fig. 2(a,iii) and (b,iii)) allow us to determine the magnetic moment of each molecule and the exchange and dipolar coupling energy. For the (3, 4) dimer shown in Fig. 2(a,i), we obtained μ_1 = 1.006 μ_B, μ_2 = 0.983 μ_B, J = 135 MHz, D = 15 MHz; for the (0, 5) dimer shown in Fig. 2(b,i), we obtained μ_1 = 1.011 μ_B, μ_2 = 0.991 μ_B, J = 54 MHz, D = 10 MHz.

Notably, when B_{tip} cancels the difference of Zeeman energy of two [FePc]1- spins (*i.e.* $\delta = 2\mu_1 B_{ex} + 2\mu_1 B_{tip} - 2\mu_2 B_{ex} = 0$, α = 1), $|10\rangle$ and $|01\rangle$ are equally weighted in states $|-\rangle$ and $|+\rangle$ and the difference between f_2 and f_3 becomes: $f_3 - f_2 = -\frac{3}{2}D(1 - 3\cos^2\theta)$. This means f_1 and f_4 have the same intensity and f_2, f_3 merge into one peak when the dipolar coupling contribution D becomes negligible. To extract the coupling strength of a two-spin system in a simpler way, we can read the ESR splitting Δf between f_1 and f_2, f_3 and f_4:

$$\Delta f = f_2 - f_1 = f_4 - f_3 = J + D(1 - 3\cos^2\theta),$$

which is independent of the tip field. Thus, we can extract the exchange and dipolar coupling constant J and D simply by fitting the ESR splitting as a function of external field direction with respect to the sample plane (Fig. 3(b)).

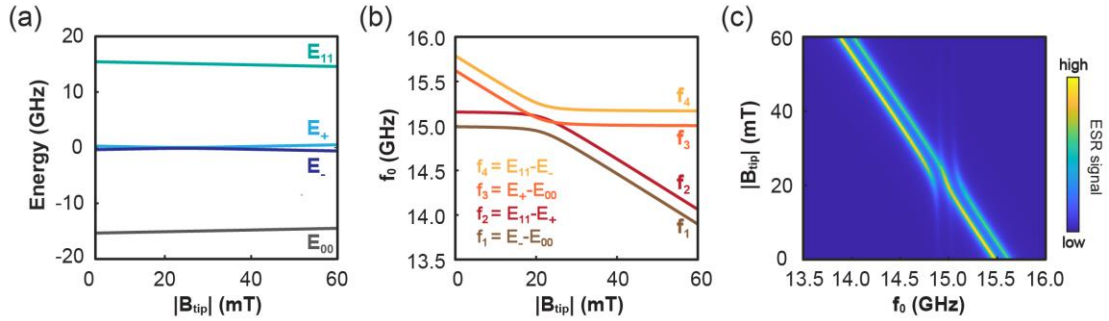

Supplementary Fig. 6 | (a) Modelled energy levels of the four spin states in a dimer as a function of tip field. (b) Corresponding frequencies of four possible ESR transitions which is calculated from energy levels shown in (a). (c) Simulated ESR spectra as a function of tip field plotted in color scale. Model parameters were selected as: μ_1 = 1.02 μ_B, μ_2 = 0.98 μ_B, $B_{ex} = B_z$ = 550 mT, B_{tip} = -60~0 mT, T = 1.7 K, J = 150 MHz, D = 15 MHz, ESR linewidth Γ = 30 MHz.

6. [FePc]$^{1-}$-[FePc]$^{1-}$ dimers with closer ligand-ligand distance

In addition to the dominant [FePc]$^{1-}$ dimer configuration, of which two nearest lobes are arranged in (2, 1) (like those shown in Supplementary Fig. 4), we also found dimers having closer ligand-ligand distance, as shown in Supplementary Fig. 7. The (5, 1) dimer in Supplementary Fig. 7(a) has a center-center distance of 1.48 nm, slightly larger than the (0, 5) dimer, 1.45 nm. However, the two nearest lobes are arranged in (2, 0) configuration and thus has closer ligand-ligand distance than the (0, 5) dimer with (2, 1) lobe-lobe configuration (Supplementary Fig. 4(d)). This gives rise to an enhanced coupling strength, 105 MHz, of the (5, 1) dimer (Supplementary Fig. 4(b)) compared to an averaged coupling energy, 64 MHz, of the (0, 5) dimer (Supplementary Fig. 5).

Supplementary Fig. 7(c) and (e) display two (5, 3) dimers of same center-center distance (1.69 nm) but very different lobe-lobe configuration, (0, 2) and (1, 1), respectively. For the (5, 3) dimer with (0, 2) lobe-lobe configuration, the center-center distance is too far to generate a measurable coupling interaction between two molecules with our ESR linewidth of about 30 MHz under these conditions. Reflected in the ESR spectrum, only a single peak can be resolved (Supplementary Fig. 7(d)). In contrast, when the two molecules are arranged in a much closer (1, 1) lobe-lobe configuration (Supplementary Fig. 7(e)), the intermolecular coupling is prominently enhanced to 145 MHz (Supplementary Fig. 7(f)). The measurements of these specific $[FePc]^{1-}$ dimers with closer ligand-ligand distance strongly indicate that the spin distribution on molecular ligands influences spin-spin interaction. However, these kinds of dimers were rarely found likely due to the stronger repulsive force by the peripheral hydrogen atoms when two lobes are closer to each other.

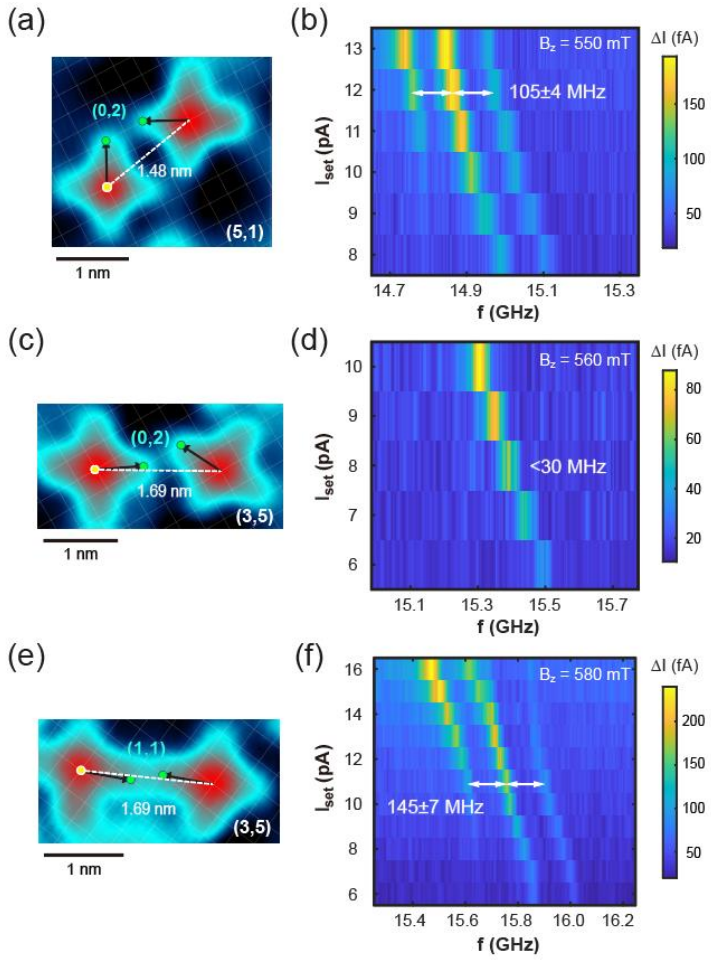

Supplementary Fig. 7 | (a) STM images of a (5, 1) dimer with (0, 2) lobe-lobe configuration and (c)(e) two (5, 3) dimers with (0, 2) and (1, 1) lobe-lobe configuration, respectively. (b)(d)(f) Corresponding current dependence ESR spectra plotted in color scale. The coupling energy for each dimer is 105±2 MHz, <30 MHz and 145±6 MHz, respectively. The tip was positioned on the yellow spots marked in STM images. Only out-of-plane field was applied during ESR measurements. Scanning conditions: (a)(c) V = 200 mV, I_{set} = 20 pA; (c) V = 150 mV, I_{set} = 8 pA. ESR conditions: V = 100 mV, (b) V_{rf} = 35 mV; (d) V_{rf} = 20 mV; (f) V_{rf} = 36 mV.

7. Fitting of J as a function of Ti_B-Fe distance and Ti_B-ligand distance

By measuring 14 $[FePc]^{1-}$-Ti_B pairs, we observed clear decay of J as both Fe center-Ti_B distance (r) and ligand-Ti_B distance (l) increases, as shown in Supplementary Fig. 8(a) and (b). Fe center in the molecule is denoted as (0, 0)) and l is the lateral distance between Ti_B atom and the ligand center. By assuming l and r are two irrelevant variables and the coupling energy J varies exponentially as a function of both r and l, we use the following equation to fit the experimental data (J_0 is set as 1 MHz to unify the unit and simplify the fit):

$$J(r,l) = J_0(c_1 \cdot e^{-r/\lambda} + c_2 \cdot e^{-l/\lambda}).$$

The (1.42, 0.71) site was chosen as a center of ligand after trying with a series of different lattice sites along the (2, 1) direction in the fit and comparing the ratio of c_1 and c_2 with spin distribution on center (71%) and ligand (<7% for each) and center suggested by DFT results, as shown in Supplementary Figs. 8(c)-(e).

Thus, the relation between l and the center-center distance r, the angle between ligand axis and connection of Ti_B-Fe (φ) is $l = \sqrt{(r\sin\varphi)^2 + \left(r\cos\varphi - \sqrt{(0.71)^2 + 1.42^2)} \cdot 0.29\right)^2}$.

Here, the coupling between Ti_B and the second nearest ligand is ignored due to the much larger distance. The fitting parameters are obtained as $c_1 = 2.63\times10^{10}$, $c_2 = 8.25\times10^{8}$, $\lambda = 0.0506$ nm (Supplementary Fig. 8(c)-(f)) and can reproduce the experimental results with great precision (Supplementary Fig. 8(g)). Supplementary Fig. 8(h) manifests clearly the two-dimensional decay of J with increasing r and l.

Since J can be written also as

$$J(r,\varphi) = J_0(c_1 \cdot e^{-r/\lambda} + c_2 \cdot e^{-\sqrt{(r\sin\varphi)^2+\left(r\cos\varphi-\sqrt{(0.71)^2+1.42^2}\cdot0.29\right)^2}/\lambda}),$$

by varying φ from 0 to π/4 and applying reflection and rotation manipulation according to molecular axes, we can simulate the spatial evolution of J with the nearby atom spin occupying different sites around the molecule. The simulated spatial energy map (colored contours in Fig. 5) agrees well with the experimental data (colored dots in Fig. 5), showing an energy valley along the 45° molecular symmetry axis where l is maximized with the same r.

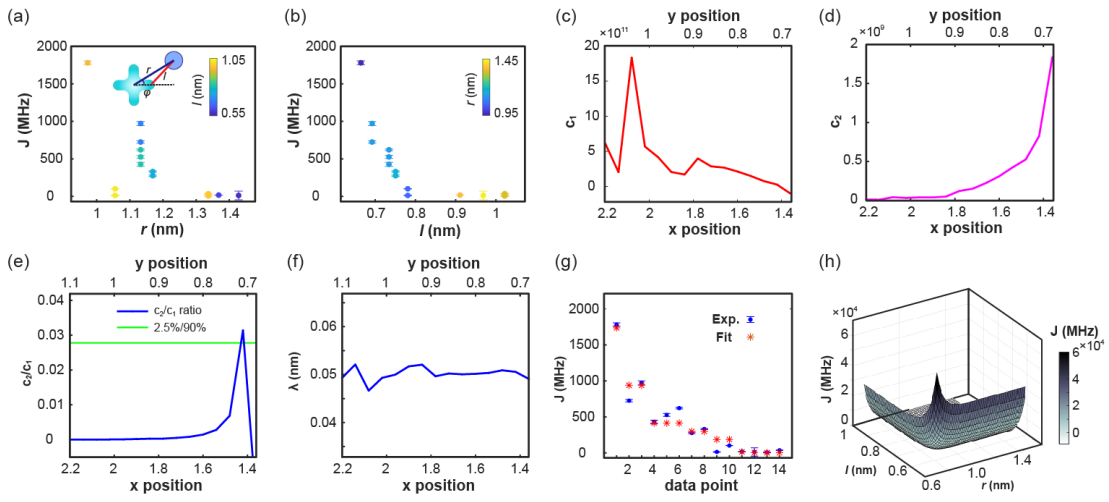

Supplementary Fig. 8 | (a) Exchange coupling energy (J) as a function of Fe-Ti_B distance r. Pairs with

different Ti_B-ligand distance l (from Ti_B to the (1.42, 0.71) lattice site) are distinguished in color scale. Inset: definition of r, l and φ. φ is the angle between the connection of Fe-Ti_B and molecular axes. (b) J as a function of l. Corresponding r of each data point is expressed in color scale. (c)(d) Fitted c_1 and c_2 as a function of different lattice sites. (e)(f) Fitting parameters as a function of different lattice sites. (g) Comparison between experimentally measured J of 14 $[FePc]^{1-}$-Ti_B pairs and fitted J by using two-variable exponent function. (h) Simulated two-dimensional decay of J as a function of r and l.

8. Details of DFT calculations

All density functional theory (DFT) calculations were performed using Quantum Espresso (version 6.5) which implements DFT using plane waves and pseudopotentials[41,42]. Pseudopotentials were chosen based on the SSSP library and the basis set was expanded using a kinetic cutoff of 40 Rydberg[43]. All pseudopotentials use the generalized gradient approximation of Perdew, Burke, and Ernzerhof (PBE) and we treat van der Waals interaction using Grimme's D3[44,45].

We first confirmed that DFT accurately reproduces the experimentally found S = 1/2 of $[FePc]^{1-}$ on MgO/Ag(100) surface. The system is modelled as 4 monolayers (ML) of silver capped by 2 ML of MgO exposing the (100) surface. Details about the setup and convergence of the MgO/Ag(100) system can be found in Ref. 509. The structure is expanded into a lateral supercell of 2×2 nm^2 which separates the $[FePc]^{1-}$ molecule by more than 6 Å from its periodic images. In the z-direction, the cell is padded with 12 Å of vacuum. Our calculations indicate that the relaxed configuration with a (2, 1) lobe orientation is indeed the lowest energy configuration and the Fe sits 2.7 Å above the oxygen (Supplementary Fig. 9(b)). An analysis of the local density of states (LDOS) (Supplementary Fig. 9(a)) confirms that the $[FePc]^{1-}$ is negatively charged (*i.e.* $FePc^{1-}$) with respect to its neutral electronic configuration in vacuum and adopts an electronic configuration $(a_{1u})^2 (e_g)^4 (b_{2g})^2 (a_{1g})^1$ with one unpaired excess electron in a dz^2 type orbital. Further analysis of the frontier orbital indicates that it consists of 71% dz^2 and <30% contributions from the ligands. This sharp charge transition is characteristic for molecules decoupled from a metal support by insulating layers[51]. In comparison, while the spin density spreads significantly along the molecular ligands (Supplementary Fig. 10(a)), the spin-1/2 hydrogenated titanium atom adsorbed on O-O bridge site (Ti_B) has very compact spin density around the atom center (Supplementary Fig. 10(b)). Therefore, a Ti_B atom can be considered as a point magnet.

Furthermore, we confirmed that charging the cell with an excess electron and removing the silver gives an identical $FePc^{1-}$ configuration on the molecule. Therefore, we were able to remove the silver in subsequent calculations which gives a considerable speedup.

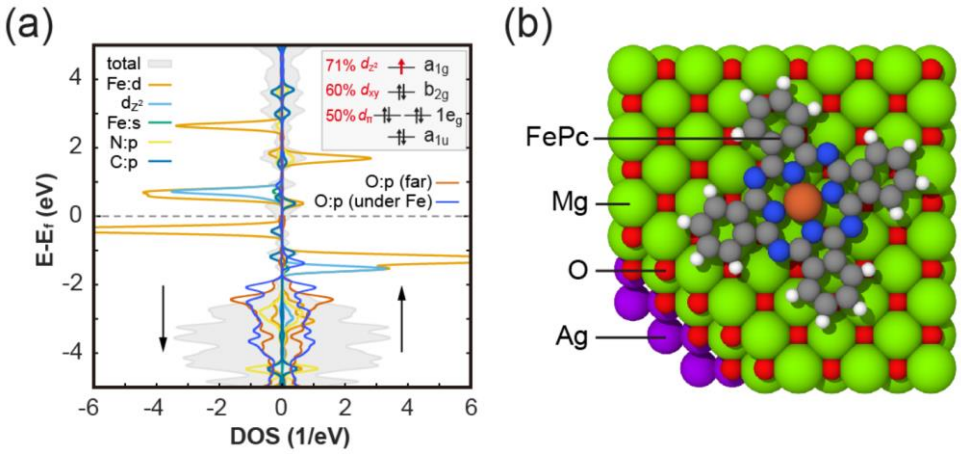

Supplementary Fig. 9 | (a) Local DOS of the $[FePc]^{1-}$ molecule on MgO/Ag(100) highlighting the unpaired dz^2 orbital. The oxygen states are separated into two cases: the oxygen atom far away from the molecule (brown line) and the oxygen atom right underneath the central Fe atom (dark blue line). Inset: electron occupancy and d components of molecular frontier orbitals. $d_\pi = 0.5(d_{zx} + d_{zy})$. The a_{1u} orbital has no contribution from d component. (b) Computational setup of an individual $[FePc]^{1-}$ on MgO surface atop an Ag(100) substrate.

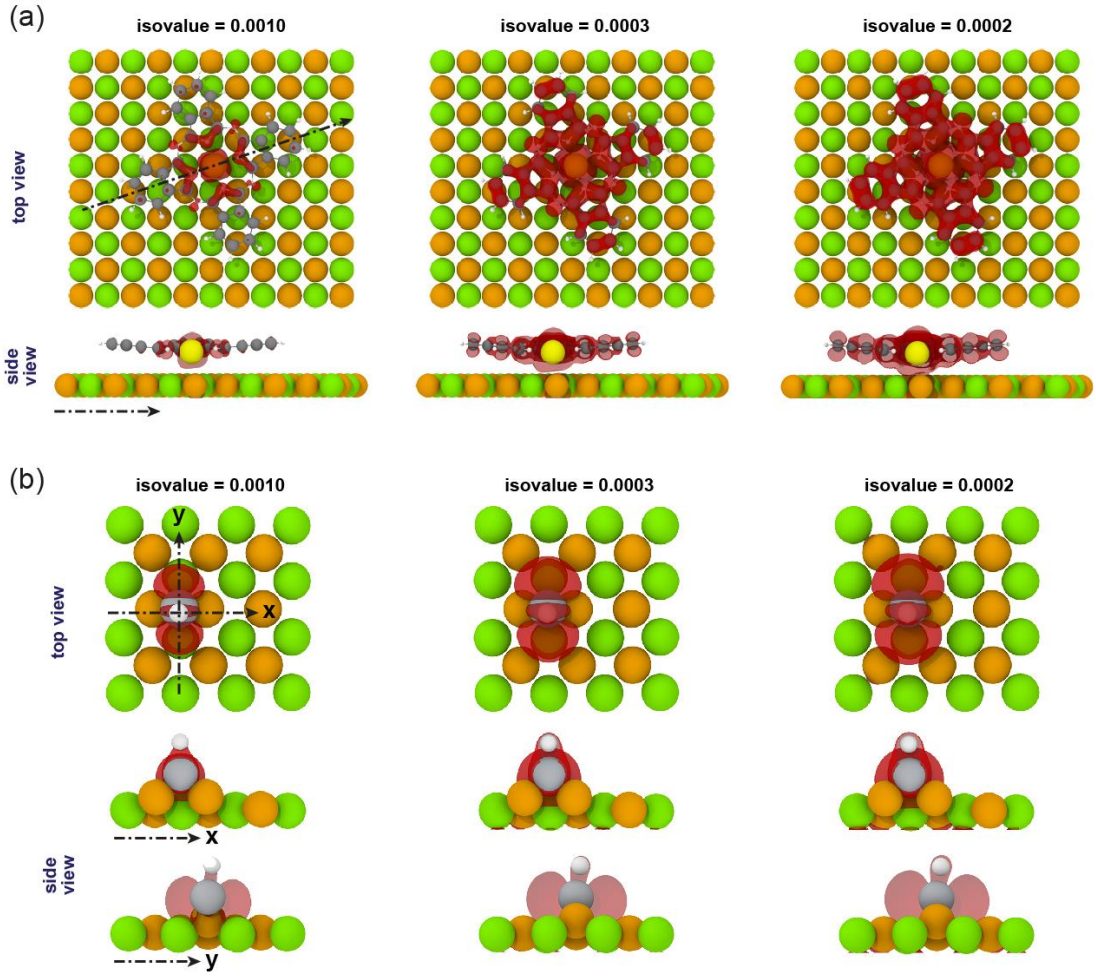

Supplementary Fig. 10 | Spin density isosurface plot of (a) a $[FePc]^{1-}$ molecule and (b) a Ti_B atom on MgO surface with different isovalues. (a) indicates the spin density distributed on both $[FePc]^{1-}$ center

and outer ligands while in (b) the spin density of a Ti_B atom is highly localized. Upper panel: top view. Lower panel: side view cleaved along the dashed lines.

In the $[FePc]^{1-}$-$[FePc]^{1-}$ dimer case, to accommodate both molecules, the cell is laterally expanded to make sure that the separation of dimers and their periodic image is at least 5 times larger than the inter-dimer distance. This is based on the assumption that the dimer interaction is dominated by static exchange that decays exponentially in vacuum. Convergence tests with larger cells indicate that this separation is sufficient to remove spurious effects due to periodic boundary conditions. Due to the single-determinant nature of the Kohn-Sham (KS) auxiliary wave-functions used in DFT, we don't have direct access to the singlet/triplet basis and rely on the broken-symmetry approach introduced by Noodleman[35]. In brief, this approach maps the KS energies of the high-spin ($m_s = 1$) and the broken symmetry ($m_s = 0$) state to the diagonal elements of the Heisenberg Hamiltonian. This method has known limitations; however, they have also been shown to give reliable results in the limiting case of two spin-1/2 centers with vanishing overlap of orbitals (*i.e.* the case of fully localized electrons at long distances), but is known to likely give unphysical results when the two spin centers are located on the same molecular units, *e.g.* in the case of biradicals[52,53].

To investigate the difference in exchange coupling for all observed dimer configuration, we calculated the energy difference between the high spin (corresponding to FM coupling) and broken symmetry (AFM coupling) configuration for a set of geometries where one [FePc]1- molecule is slightly rotated around its Fe center whilst the other is kept fixed (Supplementary Fig. 11(a)). This does not change the Fe-Fe distance but changes the ligand-ligand distance as shown in Supplementary Fig. 11(b). We then calculated the exchange coupling strength when the molecule is rotated by an angle of ϕ (Supplementary Fig. 11(c)). When the energy difference is plotted as a function of the minimum ligand-ligand distance ($d_{\min}$), a clear exponential dependence is found (Supplementary Fig. 11(d)). This is a strong indicator that the dominant mechanism here is exchange mediated by the ligands which contribute less than 30% to the frontier orbital as discussed earlier. The subtle difference in ligand-ligand distance for each observed dimer configuration then explains the difference in observed exchange coupling strength. Focusing on the (3, 4) and (0, 5) configurations as shown in Supplementary Fig. 11(d), we find that in both cases the interaction energy decays exponentially $\sim\exp(-d_{\min}/\lambda)$ with a characteristic length of λ = 0.0345 nm, a value very similar to previous calculations of the exchange interaction decay length for nickelocene[36]. We note that the decay of the exchange interaction in a molecular dimer on MgO surface is lower than in vacuum ($\lambda \sim 0.044$ nm), indicating a screening effect of the MgO layers.

Using the computationally optimized (also experimentally observed) (2, 1) lobe configuration for the (3, 4), (0, 5) and (2, 5) dimer arrangements, DFT calculation gives exchange coupling strengths in good agreement with the experimental value (Supplementary Fig. 11(e), same as Fig. 3(d)). We note that based on previous studies, this agreement in the μeV (MHz) energy range is somewhat coincidental, as differences up to a factor of 5 in the exchange energy can be routinely observed when changing the exchange-correlation functional[54]. Whilst the absolute values might therefore be subject to cancellation of errors in the calculation, the trends observed between different dimer configurations should be reliable and are in line with experimental results.

In the main text and above discussion, we intensively chose the outer hydrogen atoms for denoting the distance between two molecules. As a comparison, we also chose the distance between the centers of the benzene rings on two ligands as d_{min} and plotted the change in calculated exchange coupling energy (Supplementary Fig. 12(b)). It can be seen that the exchange coupling energy shows similar decayed behavior as the distance between two benzene centers increases compared to the case where the distance between two hydrogen atoms is chosen (Supplementary Fig. 12(a)). Given the better data quality of using H-H distance, in the main text we showed the DFT results of choosing the outer H atoms for the distance between two molecules.

In conclusion, the difference in observed exchange energy for different dimer configurations can be explained sufficiently well by their minimum ligand-ligand distance indicating that the exchange measured at the molecule center is mediated by the tails of the wave-function on the ligands.

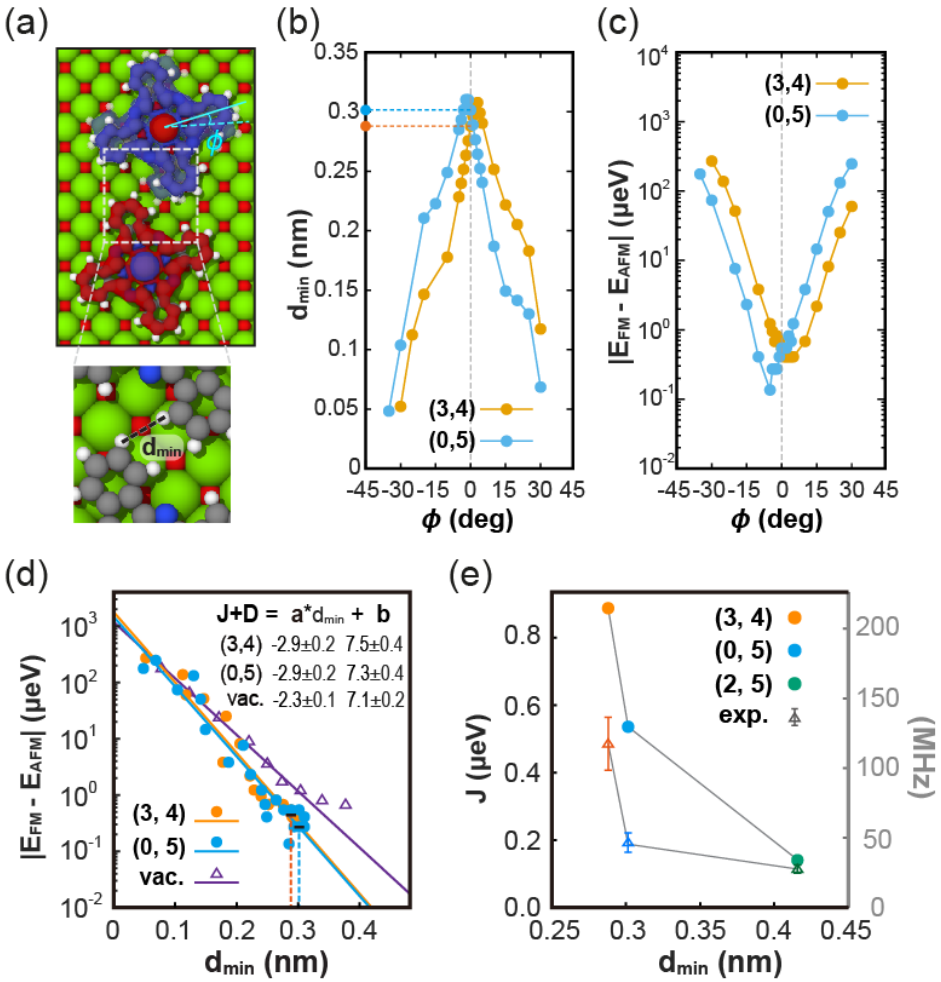

Supplementary Fig. 11 | (a) Upper panel: AFM coupled (m_s = 0) $[FePc]^{1-}$-$[FePc]^{1-}$ dimer in (3, 4) configuration on MgO. During calculation, the upper $[FePc]^{1-}$ is rotated concentrically by an angle of ϕ while the lower one is fixed. The spin-polarization isosurface is shown here (red: positive, blue: negative). Lower panel: definition of our minimal ligand-ligand distance (d_{min}) metric used to calculate the decay of exchange energy. (b) Variation of d_{min} as a function of ϕ. (c)(d) Calculated energy difference between FM and AFM coupling as function of ϕ and d_{min}, respectively, for (3, 4) and (0, 5) configuration. The

case for a dimer in vacuum (shorted as vac.) is shown for reference in (d). (e) Comparison of calculated and experimentally measured exchange coupling energy of different dimer arrangements. The experimentally measured exchange coupling energies were obtained by subtracting the dipolar contribution (considering two point spins with 1 μ_B) from the ESR splitting (17 MHz for (3, 4) and (0, 5) dimers and 14 MHz for (2, 5) dimer). (c) is the same plot as Fig. 3(d) in the main text but in linear scale.

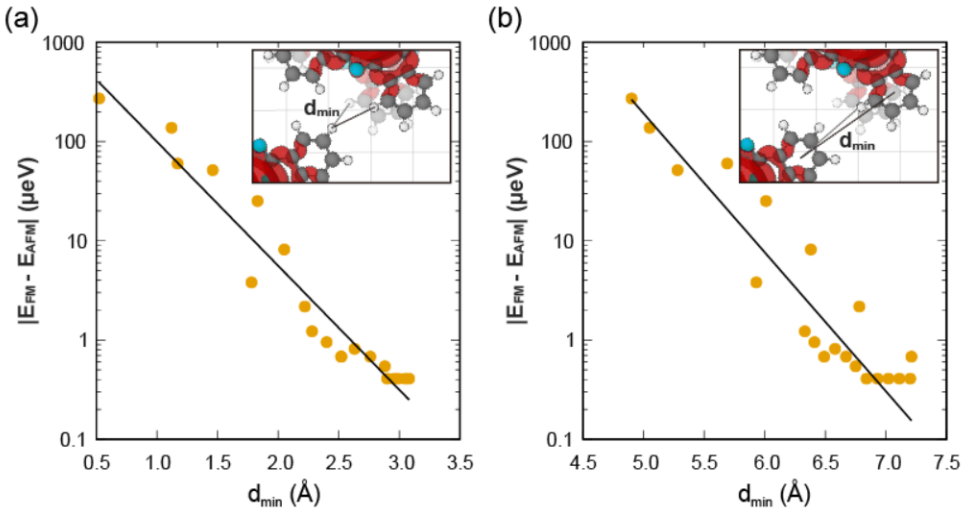

Supplementary Fig. 12 | (a) Calculated exchange coupling energy as a function of d_{min} when d_{min} is defined as the distance between two nearest hydrogen atoms of two close-by ligands. Inset: sketch showing the definition of d_{min}. (b) Calculated exchange coupling energy as a function of d_{min} when d_{min} is defined as the distance between the centers of two benzene rings on two close-by ligands. Inset: sketch showing the definition of d_{min}. The calculations were performed on a (3, 4) dimer.

9. Sample morphology

The thickness of the MgO film we prepared on Ag(100) substrate varies from 2 to 4 ML. The MgO patches grow with excavating Ag terraces and we always observed MgO patches surrounded by irregular Ag terraces, as shown in Supplementary Fig. 13. The nominal coverage of MgO patch over the entire sample surface is about 0.6 ML. The 2 ML MgO patches can be easily found and usually cover large area. All of our experiments were performed on 2 ML MgO.

It is worth noting that the FePc molecules were deposited onto the sample at room temperature while the metal atoms were deposited onto cold sample (<40 K). This results in sufficient molecular immigration and suppressed atom mobility. As a consequence, the FePc molecules were mostly found on MgO patches while the metal atoms distributed with similar coverage on both MgO and Ag terraces. We deposited the FePc molecules with a very low coverage, about 0.04 ML on MgO. However, we could still find lots of naturally formed FePc dimers, verifying the mobility of FePc molecules on surface before transferred to the experiment temperature of 2 K.

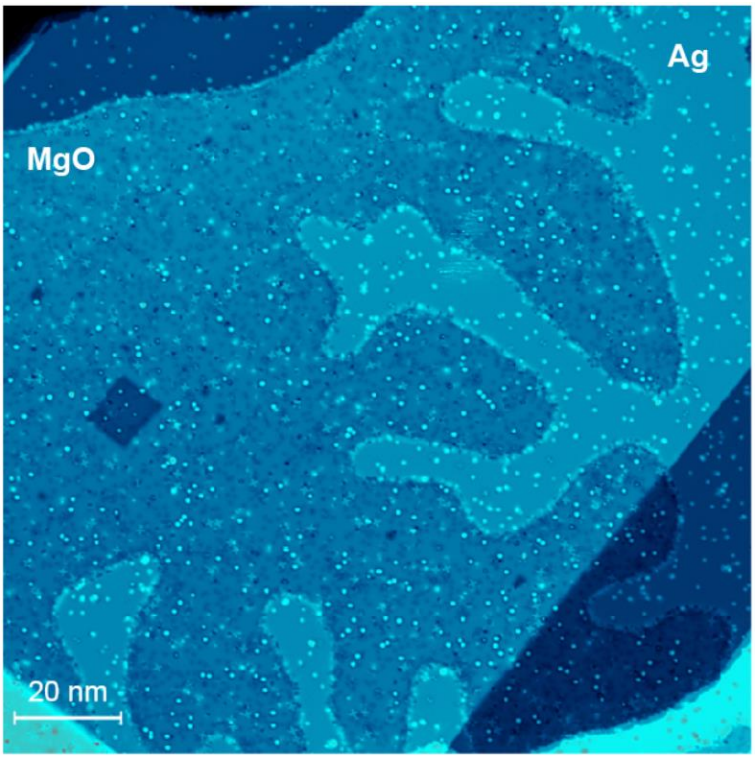

Supplementary Fig. 13 | Large-scale STM image of a MgO patch with surrounded irregular Ag(100) terraces. Scanning tunneling condition: V = 100 mV, I = 10 pA.

We note that there are some defects (black spots) on the MgO surface, which are also frequently observed on other MgO samples[55]. However, we found that these defects neither influence the adsorption site of a FePc molecule nor the interaction energy between two molecules. As shown in Supplementary Fig. 14(b) and (f), we randomly chose two FePc dimers with (5, 0) and (3, 4) configurations, respectively. Despite the appearance of black spots nearby, all the four molecules adsorb in the optimized configuration, in which the central Fe atom sits atop oxygen atom and the ligands orient to (2, 1) direction. The ESR splitting measured on each molecule within a dimer are almost the same (Supplementary Fig. 14(a) and (e)). After picking up the molecules one by one, we were able to inspect the surface condition underneath the molecules clearly. As shown in Supplementary Fig. 14(c-d) and (g-h), the defects are at different distance and direction with respect to each molecular adsorption site, further implying the negligible influence of the surface defects on the adsorption and interaction of FePc molecules.

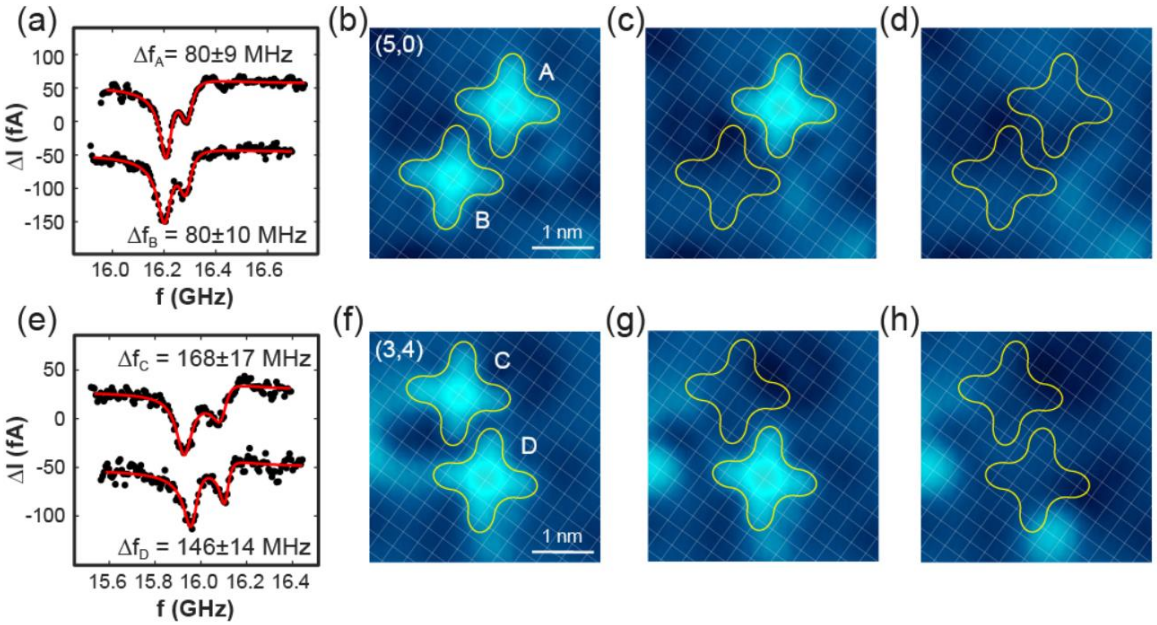

Supplementary Fig. 14 | Influence of the surface defects on molecule adsorption and ESR splitting. (a) ESR spectra (black dots) measured on the two $[FePc]^{1-}$ molecules in a (5, 0) dimer shown in (b). Red curves are the Lorentz fits. ESR conditions: V = 100 mV, $I_A = I_B$ = 19 pA; V_{rf} = 30 mV. The upper ESR spectrum is vertically shifted by 100 fA; (b)-(d) STM images of an (5, 0) dimer- before, after picking up one, and two molecules, respectively. (e) ESR spectra (black dots) measured on the two $[FePc]^{1-}$ molecules in a (3, 4) dimer shown in (f). Red curves are the Lorentz fits. ESR conditions: V = 100 mV; I_C = 27 pA, I_D = 30 pA; V_{rf} = 30 mV. The upper ESR spectrum is vertically shifted by 90 fA. (f)-(h) STM images of an (3,4) dimer, before, after picking up one, and two molecules, respectively. The measurements were performed with B_z = 600 mT. Scanning conditions: V = 100 mV, I = 20 pA.

10. Electronic properties of $[FePc]^{1-}$ on MgO

We measured the dI/dV spectrum of an individual $[FePc]^{1-}$ molecule on MgO within a large bias range to get the information of orbital states, as shown in Supplementary Fig. 15(a). Compared to the dI/dV measured on bare MgO and FePc on Ag which was reported in Ref. 19, we found the $[FePc]^{1-}$ molecule on MgO has a HOMO and LUMO at around -2 V and +1 V, respectively.

Moreover, we measured dI/dV maps of $[FePc]^{1-}$ on MgO at corresponding energies and then compared with those calculated orbital configurations of a negatively charged FePc ($[FePc]^{1-}$) on MgO and a neutral FePc ($[FePc]^{0}$) in vacuum, respectively, as shown in Supplementary Fig. 15(b). We found good agreement between the experimental dI/dV maps and the calculated orbital configurations of the $[FePc]^{1-}$ case, verifying the adsorbed FePc molecule on MgO surface is charged by one electron.

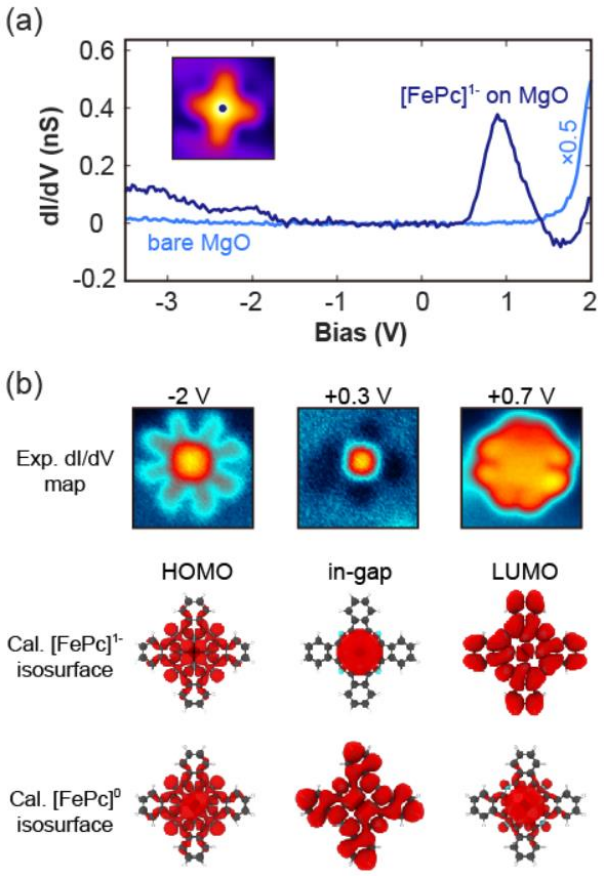

Supplementary Fig. 15 | Comparison of the experimental dI/dV maps and theoretical orbital configurations of FePc on MgO/Ag. (a) Large-range dI/dV spectrum. Inset: STM image of the $[FePc]^{1-}$ molecule used for dI/dV measurements (V = 300 mV, I = 150 pA). dI/dV spectrum was measured at the molecule center with set point of V = 2 V, I = 150 pA, V_{mod} = 10 mV. (b) Upper panel: the experimental dI/dV maps measured at different biases (constant-current mode, I = 150 pA, V_{mod} = 10 mV) corresponding to HOMO, in-gap and LUMO energy, respectively. Middle panel: the calculated orbital isosurfaces of $[FePc]^{1-}$ on MgO/Ag of HOMO, in-gap, and LUMO states. Lower panel: the calculated orbital isosurfaces of $[FePc]^{0}$ in vacuum of HOMO, in-gap, and LUMO states.

11. Analysis of the orbital configuration for different configurations of FePc and substrate

We analyzed the orbital composition for four different cases: (a) FePc in vacuum, (b) $[FePc]^{1-}$ in vacuum where the entire cell is charged by adding an electron thereby artificially reducing FePc to $[FePc]^{1-}$, (c) FePc on 4 ML Ag and (d) FePc on 2 ML MgO/4 ML Ag which represents the experiment. The results are shown in Supplementary Fig. 16 and allows us to deduce the following: $[FePc]^{0}$ (which denotes the neutral species) has a $(b_{2g})^2(a_{1u})^2(a_{1g})^2(1_{eg})^2$ orbital configuration with total spin S = 1 which upon reduction to $[FePc]^{1-}$ rearranges into $(a_{1u})^2(1_{eg})^4(b_{2g})^2(a_{1g})^1$ which is S = 1/2. The frontier orbital of $[FePc]^{1-}$ is dominantly dz^2 (85%) with further contributions from the Fe:4s orbital (13%) and ligand contributions. When adsorbed on 4 ML Ag (100) the dz^2 orbital strongly hybridizes with the silver surface owing to the spatial extent of that orbital. It is no longer possible to assign a "chemical charge state" to the molecule in this system. Its frontier orbital is a complex mixture of Fe:dz^2 and Ag states as

shown in Supplementary Fig. 17. The total charge transfer to the FePc@Ag compared to $[FePc]^0$@vacuum obtained from integrated Lowdin charges amounts to only 0.15 electrons.

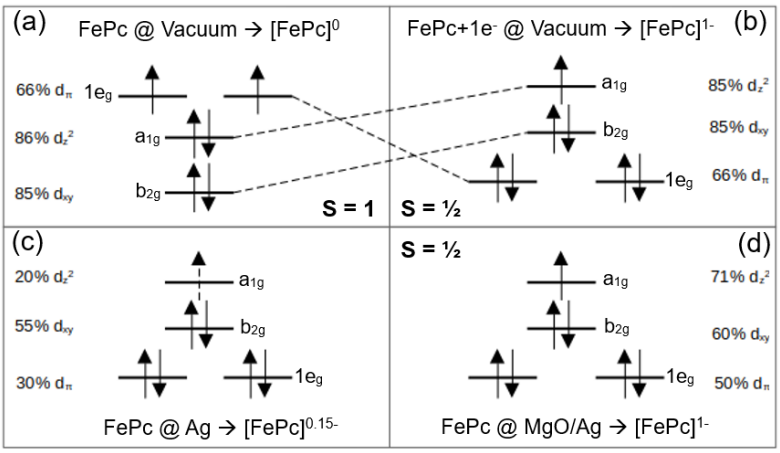

Supplementary Fig. 16 | Schematic orbital composition of orbitals with dominant Fe:3d weights near the Fermi level for four distinct cases as mentioned in the text. The orbital weight are given in percent (%) with the remaining weight to 100% being mostly ligand contributions or on-site hybridization with the Fe:4s orbital.

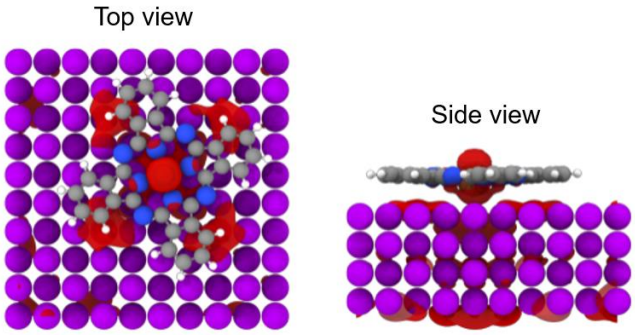

Supplementary Fig. 17 | Frontier orbital of FePc@Ag(100) showing the complex hybridization of the Fe:dz^2 and Ag orbitals.

When 2 ML of MgO are inserted between the molecule and the metal support the frontier orbital regains dz^2 character (71%). The orbital configuration for $[FePc]^{1-}$ in vacuum and FePc@Ag/MgO indicates that the molecule is in its reduced state for these two cases whilst it is in an intermediate state for FePc@Ag. This effect of a thin insulating buffer layer has been observed in other molecules as well[56].

The role of the Ag metal support is that of an electron donor to reduce the molecule, whilst the MgO buffer layer reduces hybridization with the surface and determines the adsorption geometry. To mimic the $[FePc]^{1-}$@MgO/Ag system, we place $[FePc]^{1-}$ on MgO only. This reproduces the electronic states of FePc@MgO/Ag but greatly reduces the computational cost for the larger dimer systems. The orbital configurations are shown in Supplementary Fig. 18. Moreover, a comparison between the 3d dominant orbitals of $[FePc]^{1-}$@vacuum (Supplementary Fig. 16) and $[FePc]^{1-}$@MgO (Supplementary Fig. 18) indicates a weak molecule substrate interaction since The dz^2 character of the frontier orbital is reduced by about

10% due to the hybridization with O:pz orbital.

We conclude that FePc on MgO/Ag reduces to $[FePc]^{1-}$ upon transfer of one electron from the metal support. The role of the MgO buffer layer is to reduce hybridization with the metal substrate, which mostly affects the dz^2 orbital.

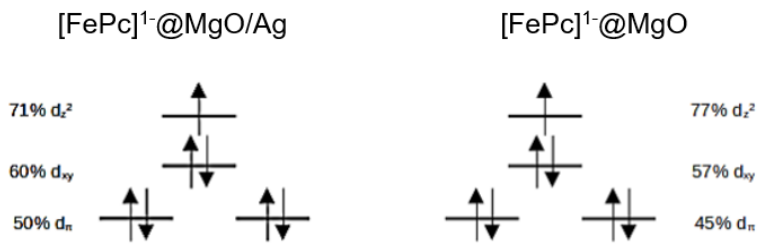

Supplementary Fig. 18 | Schematic orbital configuration of $[FePc]^{1-}$ on MgO/Ag and $[FePc]^{1-}$ on MgO. The charge state and orbital structure of these two configurations are equivalent within a few percent.

12. Anisotropy of the g-factor calculations and discussion on the origin of magnetic anisotropy

We observed that the magnetic moment of $[FePc]^{1-}$ differs by ~5% between out-of-plane and in-plane directions. A similar anisotropy in g-factor has been reported in other systems[29,30]. To verify the subtle anisotropy in the magnetic moment of $[FePc]^{1-}$, we calculated the anisotropy of the g-tensor from first principles using gauge including projector augmented wave method as implemented in QE-GIPAW[57]. We find that the calculated g-factor also shows enhancement in-plane (xx,yy) compared to the out-of-plane (zz) component. We performed calculations of $[FePc]^{1-}$@vacuum and $[FePc]^{1-}$@MgO in the (2, 1) orientation of the ligand. The results are shown in Table S1. We note that the absolute value of the g-factor is close to the free electron value (2.003), in good agreement with the experiment.

Table S1. Change in effective g-tensor components for xx, yy and zz relative to its maximum value in percentage

System	Δg^*_{xx} (%)	Δg^*_{yy} (%)	Δg^*_{zz} (%)
$[FePc]^{1-}$@vacuum	+2.3	+2.3	0.0
$[FePc]^{1-}$@MgO	+11.9	+11.9	0.0
Experiment	+5	+5	0.0

Our calculations reproduce experimental findings to a high degree. We note that these calculations are hard to converge and required cutoffs for the kinetic energy of 110 Ry.

As for the origin of the anisotropy of the g-factor, it is physically a consequence of the contribution from the d-orbital moments to the magnetic moment. Generally, for ions in solid, the ligands field lifts the degeneracies of the ground state. Consequently, this ground state must be formed of orbitals of opposite moment ($-m_l$, $+m_l$), and so has no net orbital moment. This is

the so-called quenching of the orbital moment. However, to second order in perturbation, the spin-orbit coupling mix the ground state with excited states of larger orbital moment. As a result, the g-factor takes the form $g_{ij} = 2(\delta_{ij} - \lambda\Lambda_{ij})$, where $\Lambda_{ij} = \sum_n \frac{\langle 0|L_i|n\rangle\langle n|L_j|0\rangle}{E_n - E_0}$ and $\lambda < 0$, is the spin-orbit coefficient. For the isoelectronic CoPc[29], Assour et al. explicitly calculated the g-factor anisotropy $g_{xx} = g_{zz} - 6\lambda/\Delta$ where Δ is the energy separation between orbital levels, implying $g_{xx} > g_{zz}$ as found experimentally for CoPc and in our work for $[FePc]^{1-}$ on MgO.

The comparison between the g-factor of single $[FePc]^{1-}$@MgO and bulk metal phthalocyanine systems is summarized in Table S2. In Ref. 30, the g-factor anisotropy of two distinct $[FePc]^-$ crystals, crystal I and crystal II have values of 0.134 and 0.098, respectively, very close to the value $\Delta g = 0.1$ measured by ESR-STM on single $[FePc]^-$@MgO. In Ref. 29, the g-factor anisotropy of bulk cobalt phthalocyanine (CoPc) crystals shows $\Delta g = 0.4$ and $\Delta g = 0.99$ for two distinct crystallographic structures α and β, which is significantly larger than the g-factor anisotropy of bulk $[FePc]^-$ crystal and single $[FePc]^-$@MgO. This is consistent with formula $g_{xx} = g_{zz} - 6\lambda/\Delta$ [Ref. 29] and the larger spin-orbit constant of Co^{2+} with respect to Fe^+, as shown by Dunn et al.[58], where the spin-orbit constant for Co^{2+} (Fe^+) is $\lambda =$ -515 cm^{-1} (-345 cm^{-1}), respectively.

From this table, one can also see that the average g-factor measured on single $[FePc]^-$@MgO is closer to the free electron value than measured on bulk $[FePc]^-$ crystals. While a detailed examination of this difference is beyond the scope of this manuscript, two effects can reduce the g-factor of $[FePc]^-$@MgO with respect to the bulk $[FePc]^-$ crystal.

1) The presence of MgO modifies the ligand field and so changes the mixing with the excited states of higher orbital moment. DFT calculations (Table S1) shows that the proximity of the molecule with the MgO substrate leads to a change of the g-factor. Furthermore, one can see from Ref. 30 and Table S2 that the g-factor of $[FePc]^-$ changes significantly between the two crystal I, II and $[FePc]^-$ in THF solvent. This implies that the g-factor of $[FePc]^-$ is indeed very sensitive to variations in the ligand and crystal fields. 2) The Kondo effect (Supplementary Fig. 1) may lead to a reduction of the g-factor according to the formula: $g = g_0 - J_{sd}\rho(\varepsilon_F)$ as shown theoretically[31,32] where $\rho(\varepsilon_F)$ is the density of states at the Fermi level of the silver substrate and $J_{sd} > 0$ is the antiferromagnetic exchange coupling between the conduction electrons and the magnetic moment of $[FePc]^-$.

Table S2. Experimental values of the g-factor on single $[FePc]^-$@MgO compared with g-factor measured on bulk crystal and solution of $[FePc]^-$ and CoPc by standard ESR spectroscopy.

System	g_{xx}	g_{zz}	Δg	Reference
$[FePc]^-$ @ MgO (ESR-STM)	2.116	2.016	0.100	this work
$[FePc]^-$ (crystal I)	2.487	2.353	0.134	Konarev et al. Ref. 30
$[FePc]^-$ (crystal II)	2.328	2.23	0.098	Konarev et al. Ref. 30
$[FePc]^-$ in THF	2.13	1.96	0.17	Konarev et al. Ref. 30
CoPc (α)	2.42	2.0023	0.4177	Assour et al. Ref. 29
CoPc (β)	2.9	1.91	0.99	Assour et al. Ref. 29

13. Analysis of the spin-contamination of high-spin and low-spin states

To calculate an estimate of the exchange coupling strength we calculate the energy difference between high-spin (HS) (for two spin-1/2: $s_1 + s_2 = 1$) and low-spin (or broken spin, BS) ($s_1 + s_2 = 0$) states. Due to the single-determinant nature of Kohn-Sham DFT these states are not triplet and singlet states but rather complex mixture of states[59]. In the limit of two s = 1/2 centers weakly overlapping the Noodleman formula is valid, which gives[35]:

$$J = \frac{E(HS)-E(BS)}{s_{max}^2}.$$

Since it cannot be known a priory if the condition of weak overlap and isolated s-1/2 centers is given, an alternative and more general approach, the Yamaguchi formula[60], can be used. This method takes any two states and re-normalizes their energy difference as:

$$J = \frac{E(\psi_1)-E(\psi_2)}{\langle \mathbf{S}^2\rangle_{\psi_2}-\langle \mathbf{S}^2\rangle_{\psi_1}}.$$

In special cases it has been shown that for the broken symmetry solution $\langle \mathbf{S}^2\rangle_{BS} = s_{max}$ and the denominator recovers the Noodleman formula since $s_{max} - s_{max}(s_{max}+1) = -s_{max}^2$[61].

To estimate the error introduced by DFT we calculate the spin-contamination (i.e. the deviation of s(s+1) from the expected values for singlet and triplet). In Table S3 we compare two cases: the case of $[FePc]^{1-}$ dimers in vacuum fixed at the geometry of the (3, 4) dimer and at zero degree rotation (that is the natural geometry of the (3, 4) dimer) and the case of the (3, 4) dimer adsorbed on MgO as used for the exchange calculations in the main text.

We note that for this calculation norm-conserving pseudopotentials from the ONCV suite[62] were used because of technical limitations of the program. We relaxed the entire system again with this set of pseudopotentials and found no deviation in either geometry or orbital configuration compared to the pseudopotentials used in the main text. The cutoff used here was 110 Ry with a dual of 4.

We find significant spin-contamination of the broken spin state compared to the true singlet state with values between 1.53~1.77 as expected from DFT. The denominator according to Yamaguchi however amounts to -1.19 and -1.03 (last column of Table S3), which is almost identical to Noodleman.

In all calculations the self-consistent field (SCF) convergence criterion was set to a stringent 10^{-12} Ry for the estimated SCF accuracy.

Table S3. Values for s(s+1) for the high-spin (HS) as well as the broken spin (BS) solution for $[FePc]^{1-}$ dimers in vacuum and on MgO.

System	s(s+1) (HS)	s(s+1) (BS)	Difference (BS-HS)
$[FePc]^{1-}$@vacuum	2.80	1.77	-1.03
$[FePc]^{1-}$@MgO	2.72	1.53	-1.19

14. The role of the substrate and molecular ligands on the exchange mechanism

We have calculated the exchange energy with and without MgO substrate (see Supplementary Fig. 13) to exclude that the oxygen atoms can mediate the exchange akin to superexchange in other transition metal oxides. We find no significant difference between the calculations with and without MgO other than a slower decay with increased inter-molecular distance, indicating some screening of the exchange from the substrate. It is therefore highly unlikely that the substrate plays a critical role and indicates that the exchange is very short-ranged and mediated by the ligands via close proximity. The projected DOS shown in Supplementary Fig. 9 further indicates that the low-lying Fe:3d states do not significantly hybridize with the O:2p states (which form the valence band of MgO). The DFT band-gap of MgO is under-estimated at about 4 eV, indicating that the separation might be even larger in the real system.

However, it is worth noting that the interaction between two molecular spins can occur through the involvement of fully paired orbitals of the ligand atoms, suggesting a superexchange mechanism. In order to verify superexchange interaction through the ligand, we further calculated the orbital-resolved polarization (i.e. the difference of up and down spin either per atomic shell or orbital momentum channel in case of C and H atoms representing the ligand) in Supplementary Fig. 19. Here, as discussed in the main text of Fig. 3a-b, we compare the difference in the spin polarization for the two cases - the optimized absorption geometry ($\phi = 0°$) and the geometry where one molecule is relatively rotated by 30 degrees representing a close ligand-ligand distance ($\phi = 30°$). The results show that the polarization energies of Fe:dz^2 levels of the two molecules are shifted with respect to the Fermi level (E_f) together with C:2p orbitals, which are closely located at the Fermi level (as indicated by dashed vertical lines). This reflects that the exchange interaction coupling the Fe-Fe centers is mediated via superexchange through the ligands.

On the other hand, a direct exchange means that the spin-spin interaction occurs through the orbital overlap of nearest neighboring atoms, which are H-H atoms (Fig. 3c) in our case. However, as shown in Fig. 1b, the unpaired spin is mainly distributed over the Fe center and ligands rather than the H atom at the end of the ligand. Thus, we believe that the direct exchange through H-H atom is negligible. Instead, the exchange mechanism coupling between the ligand-ligand can still occur through fully occupied orbitals of the ligand, which we identify as superexchange interaction.

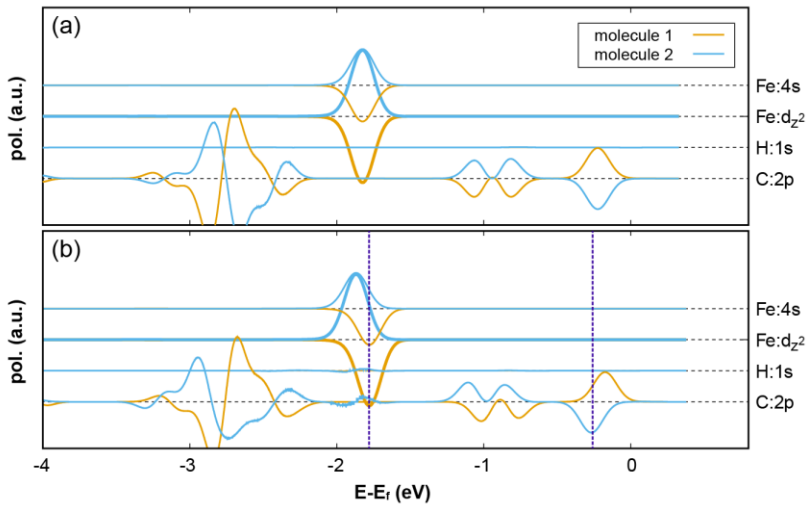

Supplementary Fig. 19 | Spin polarization per orbital type as indicated on the upper right corner for molecule 1 and molecule 2 in a FePc-FePc pair. (a) Optimized adsorption geometry (ligand-

ligand distance d = 0.289 nm). (b) Comparative geometry with molecule 2 rotated by 30 degrees (d = 0.178 nm).

15. Discussion on versatility of single-molecule ESR

Despite the large number of STM-ESR experiment reported [Ref. 12-16] in recent years, the driving mechanism of ESR in a tunneling junction of an STM is still under intense debate. So far, there are several theoretical proposals illustrating how a magnetic adsorbate responds resonantly to an applied ac electric field. For instance, 1) a modulation of the crystal field caused by the mechanical vibration of the magnetic adsorbate in an ac electric field can mix the ground state and the first-excited state and drive spin transition between the two states[14]. 2) cotunneling mechanism[63] describes that the ac electric field generates a time-dependent variation of the tunneling barrier between the magnetic adsorbate and the electrodes (tip and substrate). When an external B field is applied to the perpendicular direction of the spin quantization axis, this leads to a time-dependent variation of the transmission amplitude of the hopping between the adsorbate state and the reservoir state. As a result, a frequency-dependent dc current can be shown as an ESR signal. 3) piezoelectric coupling model[64] proposed by Lado et al. in which the ac electric field induces a mechanical vibration of the magnetic adsorbate and the time-dependent magnetic field exerted by a magnetic tip via exchange interaction with the magnetic adsorbate drives the ESR transition between the two lowest spin states.

Among the above-mentioned models, we believe that the 3) piezoelectric coupling mechanism shows the most reasonable agreement with our experiments. For any spin-1/2 species satisfying the continuous-wave ESR condition of $\Omega^2 T_1 T_2 \sim 1$, the time-dependent transverse magnetic field ($B_x(t)$) from a spin-polarized tip, which is required to drive ESR, can be given by $B_x(t) = \frac{\partial B_x}{\partial z}\Delta z(t)$. Here, $\frac{\partial B_x}{\partial z}$ is a tip magnetic field gradient in x-direction, which is perpendicular to the quantization z-axis and $\Delta z(t)$ is the time-dependent displacement amplitude of the magnetic adsorbate, which is induced by ac electric field (i.e. piezoelectric effect). It is also pointed out by Seifert et al. [Sci. Adv. 6, eabc5511 (2020)] that the ESR driving rate (Ω) is proportional to $\frac{\partial B_x}{\partial z}\Delta z$ in the case of hydrogenated Ti atoms[65]. In their work, Seifert et al. simulated the displacement amplitude (Δz) of the hydrogenated Ti atoms (S = 1/2) under a static out-of-plane electric field to be of an order of 0.5 pm/(V/nm). Our DFT calculations of $[FePc]^{1-}$ (S = 1/2) on MgO under the influence of the static out-of-plane electric field indicate a displacement amplitude (Δz) of 0.26 pm/(V/nm), which is comparable to the value found by Seifert et al.

The ESR mechanism via the piezoelectric effect requires the molecule's displacement modulation of sub-picometer scale. However, we note that the driving mechanism of STM-ESR is still under intense debate.

As shown in Fig. 1b that the ESR signal of the $[FePc]^{1-}$ originates from the unpaired electron which has a dominant dz^2 orbital configuration that contributed by the central Fe atom. As a spin 1/2 system, $[FePc]^{1-}$ on MgO has significant advantage to perform ESR measurements. Since the spin-1/2 system has much simpler magnetic properties[33], one can readily set Zeeman

energy and the corresponding frequency by tuning the magnitude of the external magnetic field. This implies that the molecular spin systems carrying spin-1/2.

For other molecular or atomic systems, we believe that ESR measurement is also adaptive as long as the system satisfies the continuous-wave ESR measurement requirements: $\Omega^2 T_1 T_2 \sim 1$ [26], where Ω is driving Rabi rate, T_1 is spin relaxation time and T_2 is spin coherence time, respectively. In general, spin number, the orbital configuration, and its coupling to a substrate, neighboring atoms and molecules will determine the three factors (Ω, T_1, T_2). However, in principle, we believe that ESR-STM technique could be used for driving spin resonance on any atomic[14,16,33] and molecular systems on surfaces when the system parameters can be tuned to meet $\Omega^2 T_1 T_2 \sim 1$. Here, we introduced the ultrathin insulating layer (MgO) to reduce the electron scattering from metal substrate, in turn, lengthening T_1 and T_2.

Another promising direction is to utilize ESR-active species such as Fe, Ti, Cu, and FePc as spin sensors (via magnetic dipolar[34] or exchange[33] interaction) to detect the magnetic properties of unknown spin systems through their magnetic interactions even though the unknown one is ESR-inactive. This also allows more versatility of the ESR-STM technique.

To give a referential spin coherence time (T_2) of $[FePc]^{1-}$ molecule used in our work to other molecular systems, here, we performed ESR measurements with varied rf amplitude (V_{rf}) at same tunneling conditions to extract the T_2 of $[FePc]^{1-}$ spin. The ESR spectra are shown in Supplementary Fig. 20(a). Based on the steady-state solution to the Bloch equations, the ESR signal can be expressed as $I = I_0 + I_{sat}\frac{\Omega^2 T_1 T_2}{1+4\pi^2(f-f_0)^2 T_2^2+\Omega^2 T_1 T_2}$. I_{sat} is the saturation current when the two spin states are driven to be equally populated. Ω is the driving Rabi rate and proportional to V_{rf}. T_1 is spin relaxation time. Thus, the ESR peak height I_{peak} ($I_{\mathrm{peak}} = I - I_0$ when $f = f_0$) can be written as $I_{\mathrm{peak}} = I_{\mathrm{sat}} \cdot \frac{\Omega^2 T_1 T_2}{\Omega^2 T_1 T_2+1}$. By fitting the ESR spectra with Lorentzian function, we can extract the ESR peak height and linewidth at each V_{rf}, as shown in Supplementary Fig. 20(b) and S20(c). Then we fit I_{peak} vs. V_{rf} using $I_{\mathrm{peak}} = I_{\mathrm{sat}}\frac{V_{rf}^2}{V_{rf}^2+\alpha}$, where $\alpha \propto (T_1 T_2)^{-1}$. We obtained the value if I_{sat} is 722.4±33.5 fA. The ESR linewidth has a relation with T_1, T_2 and Ω as $\Gamma = \frac{1}{\pi T_2}\sqrt{1+\Omega^2 T_1 T_2}$, thus can be fitted as $\Gamma = p_1\sqrt{p_2 + V_{rf}^2}$. After a simple mathematical processing, we know that the ESR linewidth has a correlation with the peak height as $\Gamma = \frac{1}{\pi T_2}\sqrt{1+\frac{1}{\frac{I_{sat}}{I_{peak}}-1}}$. Using this expression and the I_{sat} and I_{peak} obtained from above fittings, we can extract the T_2 with a value of 8.1±0.6 ns at V = 25 mV, I = 2.4 pA and B_z = 0.565 T.

Whereas it is difficult to extract the spin relaxation time (T_1) alone from the method demonstrated above, we would expect a low bound of T_1 of similar order to T_2. Moreover, we believe that by further reduce the impact of tunneling electrons[49], it is possible to lengthen the T_1 and T_2 up to hundreds of nanosecond range, which is of great potential to perform quantum manipulation-related research.

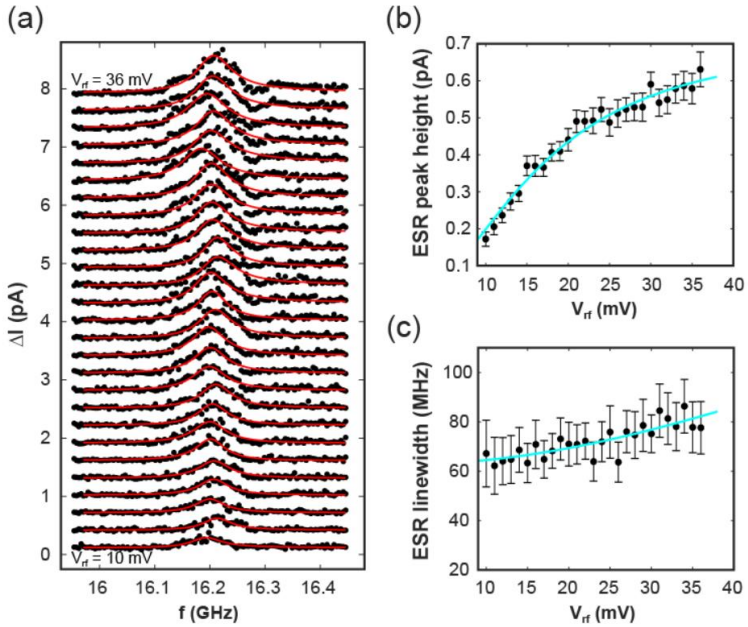

Supplementary Fig. 20 | Extraction of spin coherence time (T_2) from power-dependence ESR measurements. (a) Series of ESR spectra measured with varied V_{rf}. Each spectrum has been vertically shifted by 0.3 pA from the others for clarify. The overlapped red curves are Lorentz fits. ESR conditions: V = 25 mV, I = 2.4 pA, B_z = 565 mT. (b) Fitted ESR peak heights I_{peak} (black dots) from (a) at different V_{rf}. Cyan colored curve is the fit using $I_{peak} = I_{sat} \cdot \frac{\Omega^2 T_1 T_2}{\Omega^2 T_1 T_2 + 1}$ where I_{peak} is the ESR peak height and I_{sat} is the saturation current when the two spin states are driven to equal populations. Ω is the Rabi flop rate and is proportional to V_{rf}. (c) Fitted ESR linewidths (black dots) from (a). Cyan curve is the fit based on $\Gamma = \frac{1}{\pi T_2}\sqrt{1 + \Omega^2 T_1 T_2}$ where Γ is the ESR linewidth. By combining the expressions of I_{peak} and Γ, T_2 can be extracted as 8.1±0.6 ns. The error bars denote the 95% confidence intervals. We note that the T_2 value mentioned here is the low bound of spin coherence time.

16. Convergence of coupling energies as function of vacuum separation

We use dipole correction to remove spurious interactions of the slab with its periodic images in z-direction. To confirm convergence of our calculation with the size of vacuum, we further performed additional calculations for $[FePc]^{1-}$ dimers on MgO in the (3, 4) configuration for increasing vacuum distances and found no dependence of the calculated $E_{AFM} - E_{FM}$, as shown in Supplementary Fig. 21.

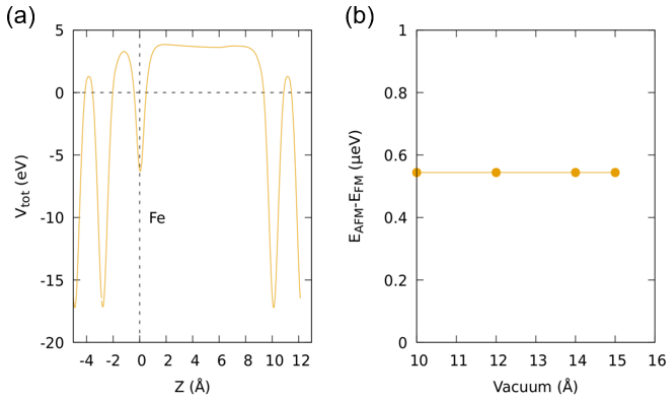

Supplementary Fig. 21 | (a) Total potential (V_{tot}) as function of the cell-height (Z) illustrating the

position of the dipole. (b) Energy difference for increasing values of vacuum showing the stability of the calculation.

17. Spatial distribution of spin signal on $[FePc]^{1-}$

As mentioned above, the Kondo feature of $[FePc]^{1-}$ on MgO surface was mainly observed around the central area. As the tip moves away from the molecule center, the signal intensity decays significantly as shown in Supplementary Fig. 22. This can be attributed to the much less distributed spin density on molecular ligands compared to the central Fe atom and an incremental difficulty of measuring a small magnetic signal at a temperature of 2 K.

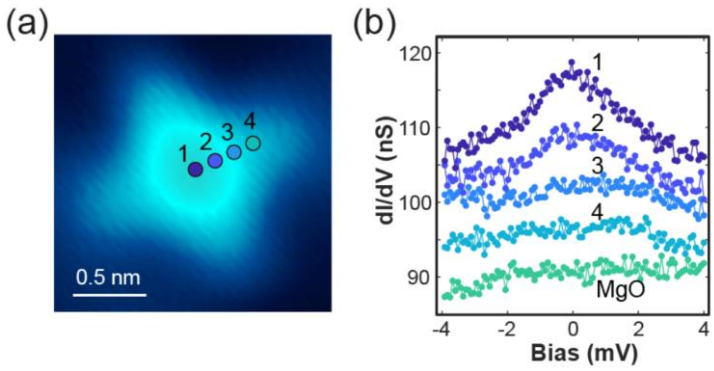

Supplementary Fig. 22 | Small-scale dI/dV spectra measured on different positions of an individual $[FePc]^{1-}$ molecule on MgO surface. (a) Zoom-in STM image of an individual $[FePc]^{1-}$ molecule. Scanning conditions: V = 100 mV, I = 20 pA; (b) dI/dV spectra measured at 4 different positions as marked by the colored dots in (a) at zero field. dI/dV conditions: V = 4 mV, I = 400 pA, V_{mod} = 0.1 mV. The spectra are vertically shifted by 5 nS for each.

We also detected the spatial distribution of ESR signal by measuring ESR spectrum at different positions on a $[FePc]^{1-}$ dimer. As shown in Supplementary Fig. 23, we could still perform ESR measurements on molecular ligands, however, with much weakened signal intensity compared to that measured at molecule center due to the small amount of spin density on the ligands. Moreover, the ESR splitting (equals to the coupling energy of the dimer) measured at different spots are almost identical, indicating the coupling energy of a molecule dimer is exclusively determined by the intermolecular geometry configurations and irrelevant to tip position. The shift of absolute resonance frequencies and number of peaks at different spots results from the varied tip field as discussed in Fig. 2.

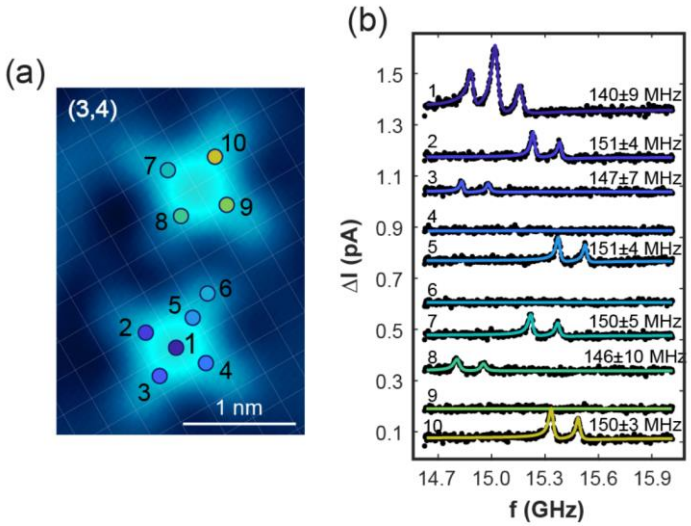

Supplementary Fig. 23 | Spatial dependence of ESR signal. (a) STM image of a (3, 4) dimer. The colored dots are corresponding to the positions where the ESR measurements were performed. Scanning conditions: V = 180 mV, I = 20 pA. (b) ESR spectra measured on different positions as marked in (a) of the $[FePc]^{1-}$ molecules in a dimer. ESR conditions: V = 100 mV, I = 12 pA, V_{rf} = 50 mV. B_z = 550 mT. Position 6 is too far from the molecule center to detect any ESR signal. For different positions, the ESR peaks appear at different frequencies because of the change in tip field.

18. Stabilization of $[FePc]^{1-}$ dimers

The adsorption energy of $[FePc]^{1-}$ on MgO (100) was calculated to be 3.4 eV/molecule. To confirm the observation of dimers, we performed DFT calculations for the (3, 4), (5, 0), (5, 1) dimer configurations on a 3 nm × 3 nm 2 ML MgO supercell. We find that the (3, 4) and (5, 0) configurations seem energetically favorable but only by about 30 meV compared to the further apart (5, 1) configuration. The (2, 1) ligand registration with respect to the substrate is protected against rotations by about 0.4 eV, which we confirmed by nudged elastic band calculations by rotating a molecule from the (2, 1) configuration to the next equivalent position, as shown in Supplementary Fig. 24.

The small energy difference between dimer configurations as well as the generally high mobility of the molecule on the MgO surfaces justifies the observed coexistence of all these dimer formations.

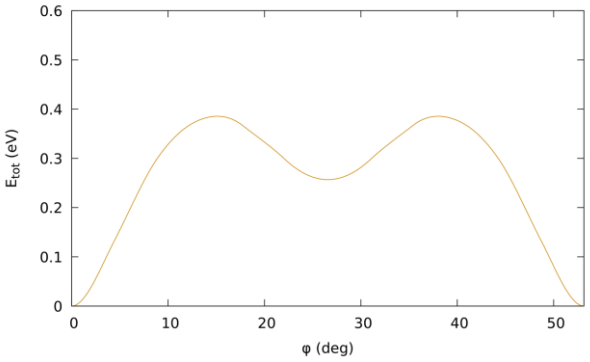

Supplementary Fig. 24 | Barrier (E_{tot}) against rotation (φ) for an $[FePc]^{1-}$ molecule on MgO between two equivalent (2, 1) ligand configurations.

19. Discussion on the orbital symmetry of Ti_B atom with respect to $[FePc]^{1-}$ molecule

Among all the experimentally observed $[FePc]^{1-}$-Ti_B dimers, we found the Ti_B atom can sit at different bridge sites with respect to the four-fold molecular axis, forming an angle between the bridge orientation and the closest molecular ligand of either 63.4° or 26.6°, as shown in Supplementary Fig. 25(a) and (c). This brings the concern of whether the two-fold orbital symmetry of the Ti_B atom along different in-plane directions[66] should be considered or not. Here, we think the influence of the two-fold axis of Ti_B atom can be neglected for the sake that: 1) The spin density of a Ti_B atom is much more localized than that of a $[FePc]^{1-}$ molecule, as shown in Supplementary Fig. 10. 2) In a hypothetical case, we assume the Ti_B atom also has spatially extended spin density according to its two-fold axis, as shown in Supplementary Fig. 25(e). Two Ti_B atoms (denoted as A and B) are set as equally far from the $[FePc]^{1-}$ center (C) but sitting at different bridge sites, named (2.5, 3) and (3, 2.5). The outer contour of atom A and B are marked as A1, A2, B1 and B2 based on the theoretical orbital configurations in Supplementary Fig. 10. However, we note that the distances between the molecule center and the outer contour of two Ti_B atoms are identical (CA1 = CB1, CA2 = CB2). There is subtle difference on the distances between the molecular ligand (L) and the outer contour of two Ti_B atoms (LA1>LA2, LB1<LB2). But this can be neglected since the spin distribution on the molecular ligand and outer contour of Ti_B atom only count a small proportion of the entire spin density. In the above regard, we neglect the two-fold axis of Ti_B atom in our work and the simulation considering only the four-fold symmetry of a FePc molecule well reproduces our experimental findings.

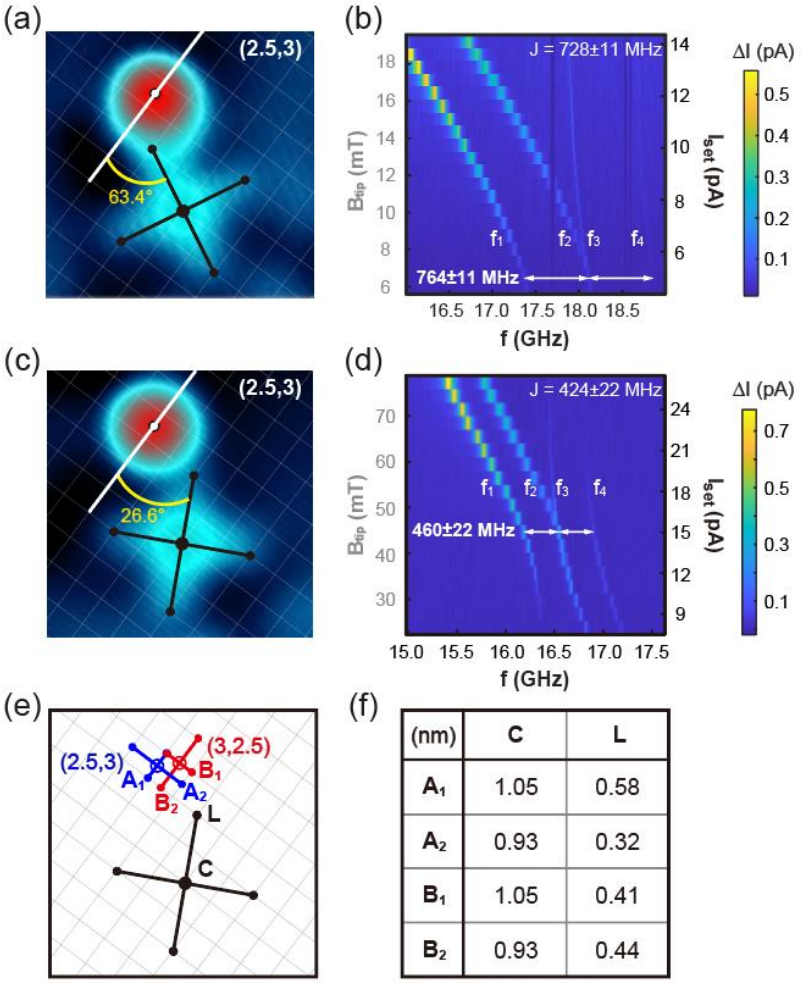

(nm)	C	L
A_1	1.05	0.58
A_2	0.93	0.32
B_1	1.05	0.41
B_2	0.93	0.44

Supplementary Fig. 25 | Negligible influence of the two-fold symmetry of Ti_B orbitals on the interaction with $[FePc]^{1-}$. (a)(c) STM images of two (2.5, 3) Ti_B-$[FePc]^{1-}$ pairs in which the closest molecule ligand points to the axis of the Ti_B atom with different angles. (b)(d) Corresponding ESR spectra measured on the $[FePc]^{1-}$ molecules in (a) and (c). (a)-(d) are same results as shown in Fig. 4(a) and 4(b) in the main text. (e) Schematic diagram of a $[FePc]^{1-}$ molecule (black cross) and two TiB atoms sitting at different bridge sites: (2.5, 3) and (3, 2.5) (blue and red empty circles) with respect to the molecule center. The molecule center is denoted as C, the closest ligand is denoted as L. The two-fold axis of Ti_B atom is reflected by marking two artificial arms (A1, A2 and B1, B2) according to the atomic orbital configurations, where A and B represent the Ti_B-$[FePc]^{1-}$ pair of (c) and (a) respectively. (f) The distances from the molecular center (C) and molecular ligand (L) to the two-fold axis of the atom (A1, A2, B1, and B2).

References

[14] Baumann, S. et al. Electron paramagnetic resonance of individual atoms on a surface. *Science* **350,** 417–420 (2015).

[16] Yang, K. et al. Electrically controlled nuclear polarization of individual atoms. *Nat. Nanotechnol.* **13,** 1120–1125 (2018).

[26] Abragam, A. & Bleaney, B. *Electron Paramagnetic Resonance of Transition Ions* (Oxford Univ.

Press, 2012).

[29] Assourlb, J. M. & Kahn W. K. Electron spin resonance of α- and β-cobalt phthalocyanine. *J. Am. Chem. Soc.* **87,** 207–212 (1965).

[30] Konarev, D. V. et al. Ionic compound containing iron phthalocyanine $(Fe^{I}Pc)^{-}$ anions and $(C_{70}^{-})_2$ dimers. Optical and magnetic properties of $(Fe^{I}Pc)^{-}$ in the solid state. *Dalton Trans.* **41,** 13841–13847 (2012).

[31] Wolf, E. L. & Losee, D. L. G-shifts in the "s-d" exchange theory of zero-bias tunneling anomalies. *Phys. Lett. A* **29,** 334–335 (1969).

[32] Barnes, S. E. Theory of electron spin resonance of magnetic ions in metals. *Adv. Phys.* **30,** 801–938 (1981).

[33] Yang, K. et al. Engineering the eigenstates of coupled spin-1/2 atoms on a surface. *Phys. Rev. Lett.* **119,** 227206 (2017).

[34] Choi, T. et al. Atomic-scale sensing of the magnetic dipolar field from single atoms. *Nat. Nanotechnol.* **12,** 420–424 (2017).

[35] Noodleman, L. Valence bond description of antiferromagnetic coupling in transition metal dimers. *J. Chem. Phys.* **74,** 5737–5743 (1981).

[36] Czap, G. et al. Probing and imaging spin interactions with a magnetic single-molecule sensor. *Science* **364,** 670–673 (2019).

[41] Giannozzi, P. et al. QUANTUM ESPRESSO: a modular and open-source software project for quantum simulations of materials. *J. Phys. Condens. Matter* **21,** 395502 (2009).

[42] Giannozzi, P. et al. Advanced capabilities for materials modelling with Quantum ESPRESSO. *J. Phys. Condens. Matter* **29,** 465901 (2017).

[43] Prandini, G., Marrazzo, A., Castelli, I. E., Mounet, N. & Marzari, N. Precision and efficiency in solid-state pseudopotential calculations. *npj Comput. Mater.* **4,** 1–17 (2018).

[44] Perdew, J. P., Burke, K. & Ernzerhof, M. Generalized gradient approximation made simple. *Phys. Rev. Lett.* **77,** 3865–3868 (1996).

[45] Grimme, S., Hansen, A., Brandenburg, J. G. & Bannwarth, C. Dispersion-corrected mean-field electronic structure methods. *Chem. Rev.* **116,** 5105–5154 (2016).

[46] Ternes, M. Spin excitations and correlations in scanning tunneling spectroscopy. *New J. Phys.* **17,** 063016 (2015).

[47] The experimental data was fit by using the program-scripts developed by Markus Ternes.

[48] Loth, S. et al. Controlling the state of quantum spins with electric currents. *Nat. Phys.* **6,** 340–344 (2010).

[49] Yang. K. et al. Coherent spin manipulation of individual atoms on a surface. *Science* **366,** 509–512 (2019).

[50] Wolf, C., Delgado, F., Reina, J. & Lorente, N. Efficient ab Initio multiplet calculations for magnetic adatoms on MgO. *J. Phys. Chem. A* **124,** 2318–2327 (2020).

[51] Hollerer, M. et al. Charge transfer and orbital level alignment at inorganic/organic interfaces: the role of dielectric interlayers. *ACS Nano* **11,** 6252–6260 (2017).

[52] Malrieu, J. P., Caballol, R., Calzado, C. J., De Graaf, C. & Guihéry, N. Magnetic interactions in

molecules and highly correlated materials: physical content, analytical derivation, and rigorous extraction of magnetic hamiltonians. *Chem. Rev.* **114,** 429–492 (2014).

[53] Ferré, N., Guihéry, N. & Malrieu, J. P. Spin decontamination of broken-symmetry density functional theory calculations: Deeper insight and new formulations. *Phys. Chem. Chem. Phys.* **17,** 14375–14382 (2015).

[54] Sheng, X., Thompson, L. M. & Hratchian, H. P. Assessing the calculation of exchange coupling constants and spin crossover gaps using the approximate projection model to improve density functional calculations. *J. Chem. Theory. Comp.* **16,** 154–163 (2020).

[55] Schintke, S. et al. Insulator at the ultrathin limit: MgO on Ag(001). *Phy, Rev. Lett.* **27,** 276801 (2001).

[56] Hollerer, M. et al. Charge transfer and orbital level alignment at inorganic/organic interfaces: The role of dielectric interlayers. *ACS Nano* **11,** 6252–6260 (2017).

[57] Varini, N., Ceresoli, D., Martin-Samos, L., Girotto, I. & Cavazzoni, C. Enhancement of DFT-calculations at petascale: nuclear magnetic resonance, hybrid density functional theory and Car-Parrinello calculations. *Comput. Phys. Commun.* **184,** 1827–1833 (2013).

[58] Dunn, T. M. Spin-orbit coupling in the first and second transition series. *Trans. Faraday Soc.* **57,** 1441-1444 (1961).

[59] Ferré, N., Guihéry, N. & Malrieu, J. P. Spin decontamination of broken-symmetry density functional theory calculations: Deeper insight and new formulations. *Phys. Chem. Chem. Phys.* **17,** 14375–14382 (2015).

[60] Yamaguchi, K., Takahara, Y. & Fueno, T. Ab-Initio Molecular Orbital Studies of Structure and Reactivity of Transition Metal-OXO Compounds. in Applied Quantum Chemistry (eds. Smith, V. H., Schaefer, H. F. & Morokuma, K.) 155–184 (Springer Netherlands, 1986).

[61] Schurkus, H. F., Chan, G. K. L., Chen, D. T., Cheng, H. P. & Stanton, J. F. Theoretical prediction of magnetic exchange coupling constants from broken-symmetry coupled cluster calculations. *J. Chem. Phys.* **152,** 18–21 (2020).

[62] Hamann, D. R. Optimized norm-conserving Vanderbilt pseudopotentials. *Phys. Rev. B* **88,** 1–10 (2013).

[63] Reina Gálvez, J., Wolf, C., Delgado, F., & Lorente, N. Cotunneling mechanism for all-electrical electron spin resonance of single adsorbed atoms. Phys. Rev. B 100, 035411 (2019).

[64] Lado, J. L., Ferrón, A. & Fernández-Rossier, J. Exchange mechanism for electron paramagnetic resonance of individual adatoms. *Phys. Rev. B* **96,** 205420 (2017).

[65] Seifert, T. S. et al. Longitudinal and transverse electron paramagnetic resonance in a scanning tunneling microscope. *Sci. Adv.* **6,** eabc5511 (2020).

[66] Veldman, L. M. et al. Free coherent evolution of a coupled atomic spin system initialized by electron scattering. *Science* **372,** 964–968 (2021).